

Optimization on Manifolds via Graph Gaussian Processes

Hwanwoo Kim¹, Daniel Sanz-Alonso¹, and Ruiyi Yang²

¹University of Chicago, ²Princeton University

Abstract

This paper integrates manifold learning techniques within a *Gaussian process upper confidence bound* algorithm to optimize an objective function on a manifold. Our approach is motivated by applications where a full representation of the manifold is not available and querying the objective is expensive. We rely on a point cloud of manifold samples to define a graph Gaussian process surrogate model for the objective. Query points are sequentially chosen using the posterior distribution of the surrogate model given all previous queries. We establish regret bounds in terms of the number of queries and the size of the point cloud. Several numerical examples complement the theory and illustrate the performance of our method.

1 Introduction

This paper investigates a manifold learning technique to solve the optimization problem

$$\text{maximize } f(x), \quad x \in \mathcal{M}, \quad (1.1)$$

where $\mathcal{M} \subset \mathbb{R}^d$ is a compact manifold and $f : \mathcal{M} \rightarrow \mathbb{R}$ is a sufficiently smooth objective function. We are motivated by applications where:

- (i) The manifold \mathcal{M} is unknown but we are given a point cloud of N manifold samples $\{x_i\}_{i=1}^N =: \mathcal{M}_N \subset \mathcal{M}$.
- (ii) The objective f is expensive to evaluate and we may only collect $L \ll N$ noisy measurements y_ℓ of the form

$$y_\ell = f(z_\ell) + \eta_\ell, \quad \eta_\ell \stackrel{i.i.d.}{\sim} \mathcal{N}(0, \sigma^2), \quad 1 \leq \ell \leq L, \quad (1.2)$$

where $\{z_\ell\}_{\ell=1}^L \subset \mathcal{M}_N$ are query points and σ is a given noise level.

Since we view the manifold \mathcal{M} as hidden and the objective f as a noisy black-box, it is infeasible to obtain analytic expressions for the differential geometric quantities appearing in first- and second-order manifold optimization algorithms [18, 1, 8, 34, 57]. For this reason, we consider a *gradient-free* Bayesian optimization approach. Our algorithm, abbreviated as GGP-UCB, incorporates a graph Gaussian process (GGP) surrogate model for the objective [45] with an upper confidence bound (UCB) acquisition function [49] to sequentially search for candidates of the optimizer.

We establish regret bounds that ensure that when the objective f is a sample from a squared exponential or Matérn GP on the manifold \mathcal{M} , the output of our GGP-UCB algorithm converges to the desired maximizer. The analysis combines (i) regret bounds for GP-UCB algorithms [49, 4]; and (ii) error bounds on the approximation of manifold GP models using GGPs defined on the given point cloud [45, 46]. Our asymptotic results suggest that taking $L \ll N$ suffices to balance both types of error. We illustrate and complement the theory with simulation studies on several manifolds.

1.1 Motivation, Contributions, and Other Related Work

Optimization problems on smooth manifolds are ubiquitous in science and engineering. In some applications the manifold is naturally determined by the problem at hand. For instance, low-rank matrix completion calls for optimization on the Riemannian submanifold of matrices of a given size and rank; principal component analysis calls for optimization on Stiefel and Grassman manifolds; and image alignment calls for optimization on the special orthogonal group of rotations, which has a natural manifold structure [1, 8]. If the manifold belongs to a limited number of families such as Stiefel, Grassman, or flag manifolds [57], the differential geometric quantities appearing in manifold optimization algorithms have analytic expressions that lead to efficient and stable implementations based on standard matrix factorizations from numerical linear algebra [18].

In contrast, in the applications that motivate our work the manifold may not belong to an agreeable family or one may only have access to a point cloud representation. For instance, manifolds arise as a consequence of low-dimensional structure in high-dimensional data, as physical constraints that may be only observed at sensor locations, and as shapes described by landmarks [33, 22, 24]. In these cases, analytic expressions for the geometric quantities appearing in first- and second-order manifold optimization algorithms are not available. This challenge is exacerbated when the objective function (i) is expensive to query due to computational, monetary, or opportunity costs; (ii) is given as a *black-box* in that one has only access to noisy output from f rather than to an analytic expression of this function; and (iii) does not satisfy structural assumptions (e.g. concavity or linearity) other than a sufficient degree of smoothness. We refer to [21] for a survey of problems where these three conditions arise.

The above considerations motivate us to adopt a Bayesian optimization approach [43, 48, 21, 9] and leverage a surrogate model for the objective to sequentially find query points. More precisely, Bayesian optimization algorithms find new query points by maximizing an *acquisition function* defined using the posterior distribution of the surrogate model given all previous queries. Acquisition functions are designed to be inexpensive to evaluate and optimize. There are many possible choices of surrogate model (e.g. GPs [55, 29] and Bayesian additive regression trees [12]) and acquisition function (e.g. expected improvement, entropy search, and knowledge gradient —see [21] for a review). While the practical implementation of Bayesian optimization methods often includes *ad-hoc* heuristics, convergence guarantees have been investigated in [49, 52, 30, 10, 14, 38]. As noted in [21], Bayesian optimization algorithms have been most popular in continuous Euclidean domains. Methods that are specifically tailored to manifold settings [35, 36] and discrete spaces [2, 42, 50, 15] have received less attention.

In this paper we investigate a discrete Bayesian optimization algorithm on a point cloud that, as opposed to [35, 36], is entirely gradient-free and does not rely on first-order manifold optimization to maximize the acquisition function. Our discrete graph-based method has the distinctive feature that both the surrogate model and the acquisition function are carefully chosen to ensure convergence to the desired maximizer under suitable smoothness assumptions on the objective; these smoothness requirements are naturally encoded by assuming that the objective is a sample from a squared exponential or Matérn GP on the hidden manifold. We consider GGP surrogate models that provably converge (as the size N of the point cloud grows) to their manifold counterparts. Our analysis of GGPs generalizes the bounds for Matérn models in [45, 46, 26, 23] to also cover squared exponential kernels. Applications of GGPs in Bayesian inverse problems, spatial statistics, and

semi-supervised learning are discussed in [45, 27, 31, 32]. Finally, our choice of acquisition function follows [49, 4] and, as we show, provably corrects the misspecification error caused by the point cloud representation of the manifold.

1.2 Outline

- Section 2 introduces the GGP-UCB algorithm and describes the choice of surrogate model and acquisition function. Our main result, Theorem 2.4, establishes convergence rates.
- Section 3 discusses important practical considerations such as estimating the parameters of the surrogate model and tuning the acquisition function.
- Section 4 contains numerical examples that illustrate and complement the theory.
- Section 5 closes with a summary of our paper and directions for further research.
- An appendix includes the proofs of our main results.

1.3 Notation

For a, b two real numbers, we denote $a \wedge b = \min\{a, b\}$ and $a \vee b = \max\{a, b\}$. The symbol \lesssim will denote less than or equal to up to a universal constant. For two real sequences $\{a_i\}$ and $\{b_i\}$, we denote (i) $a_i \ll b_i$ if $\lim_i(a_i/b_i) = 0$; (ii) $a_i = O(b_i)$ if $\limsup_i(a_i/b_i) \leq C$ for some positive constant C ; and (iii) $a_i \asymp b_i$ if $c_1 \leq \liminf_i(a_i/b_i) \leq \limsup_i(a_i/b_i) \leq c_2$ for some positive constants c_1, c_2 .

2 The GGP-UCB Algorithm

In this section we introduce our algorithm and establish convergence guarantees. We start in Subsection 2.1 by formalizing the problem setting. Subsection 2.2 describes the main GGP-UCB algorithm. The choice of surrogate model and acquisition function are discussed in Subsections 2.3 and 2.4, respectively. Finally, Subsection 2.5 presents our main theoretical result, Theorem 2.4.

2.1 Problem Formulation

Let f be a function defined over a compact Riemannian submanifold $\mathcal{M} \subset \mathbb{R}^d$ of dimension m . Suppose that a full representation of \mathcal{M} is not available and we are only given the dimension m and a point cloud of manifold samples $\{x_i\}_{i=1}^N =: \mathcal{M}_N \subset \mathcal{M}$. Evaluations of f are assumed to be expensive and corrupted by an independent additive Gaussian noise $\mathcal{N}(0, \sigma^2)$ with known noise level σ , as in (1.2). The goal is then to optimize $f_N := f|_{\mathcal{M}_N}$, the restriction of f to \mathcal{M}_N , with few queries of f .

Let $\mathcal{Z}_L := \{z_\ell\}_{\ell=1}^L \subset \mathcal{M}_N$ denote the query points sequentially found in the first L iterations of our algorithm, introduced in Subsection 2.2 below. We shall quantify the performance of our approach using the *simple regret*, defined as

$$r_{N,L} = f(z^*) - f(z_L^*), \quad z^* = \arg \max_{z \in \mathcal{M}_N} f(z), \quad z_L^* = \arg \max_{z \in \mathcal{Z}_L} f(z). \quad (2.1)$$

Note that the simple regret depends both on the number L of queries and on the size N of the point cloud, since z^* and z_L^* both depend implicitly on N . One should interpret N as a large fixed number and L as the running index. The dependence on N of the query points z_ℓ 's will be omitted for notational simplicity.

Remark 2.1. The optimizer over the point cloud \mathcal{M}_N is not necessarily the global optimizer of f over \mathcal{M} . Since we only have access to \mathcal{M}_N , finding the maximizer over \mathcal{M}_N is the best we can hope for without reconstructing or estimating the hidden manifold \mathcal{M} . For sufficiently large N , the point cloud provides sufficient geometric information to optimize a smooth objective. For instance, [25, Theorem 2] shows that if the x_i 's are i.i.d. samples from a suitable probability measure on \mathcal{M} , then with high probability the point cloud forms a ρ_N -net over \mathcal{M} with $\rho_N \rightarrow 0$, i.e.,

$$\min_{i=1,\dots,N} d_{\mathcal{M}}(z, x_i) \leq \rho_N \quad \forall z \in \mathcal{M},$$

where $d_{\mathcal{M}}$ denotes the geodesic distance. Therefore for smooth f 's we will obtain an approximate global optimizer, in the sense that

$$f(z^*) - f(z_N^*) = f(z^*) - f(\tilde{z}_N^*) + f(\tilde{z}_N^*) - f(z_N^*) \leq f(z^*) - f(\tilde{z}_N^*) \xrightarrow{N \rightarrow \infty} 0,$$

where $z^* = \arg \max_{z \in \mathcal{M}} f(z)$, $z_N^* = \arg \max_{z \in \mathcal{M}_N} f(z)$ and $\tilde{z}_N^* = \arg \min_{z \in \mathcal{M}_N} d_{\mathcal{M}}(z^*, z)$. For this reason, we shall focus on optimizing f over \mathcal{M}_N in the rest of the paper. \square

2.2 Main Algorithm

The Bayesian approach to optimization starts by constructing a GP model for the function to be optimized. We recall that a GP with mean $\mu(\cdot)$ and covariance $c(\cdot, \cdot)$ is a stochastic process where the joint distribution over any finite set of indices s_1, \dots, s_n is a multivariate Gaussian with mean vector $[\mu(s_i)]_{i=1}^n$ and covariance matrix $[c(s_i, s_j)]_{i,j=1}^n$ [55]. The mean and covariance functions together encode information about the values of the function, their correlation, and their uncertainty.

In our setting, we need to construct a GP surrogate prior model π_N for f_N , where π_N would simply be an N -dimensional multivariate Gaussian. A natural requirement is that, for $u_N \sim \pi_N$, $u_N(x_i)$ and $u_N(x_j)$ should be highly correlated iff x_i and x_j are close *along the manifold*, that is, if the geodesic distance $d_{\mathcal{M}}(x_i, x_j)$ is small. We shall discuss in Subsection 2.3 prior models π_N that fulfill this requirement. Defining the covariance matrix of π_N by using a standard covariance function in the Euclidean space \mathbb{R}^d would in general fail to meet this requirement, since two points may be close in Euclidean space but far apart in terms of the geodesic distance $d_{\mathcal{M}}$ in \mathcal{M} . We refer to Subsection 4.2 and Figure 4a for an illustrative example.

Once a choice of surrogate prior model is made, the next step is to sequentially find query points by maximizing an acquisition function [49]. Suppose we have picked query points $z_1, \dots, z_{\ell-1}$ in the first $\ell - 1$ iterations and obtained noisy measurements

$$y_k = f(z_k) + \eta_k, \quad \eta_k \stackrel{i.i.d.}{\sim} \mathcal{N}(0, \sigma^2), \quad 1 \leq k \leq \ell - 1. \quad (2.2)$$

At the ℓ -th iteration, we will pick the next query point z_{ℓ} by maximizing an upper confidence bound acquisition function [49, 4] of the form

$$A_{N,\ell}(z) = \mu_{N,\ell-1}(z) + B_{N,\ell} \sigma_{N,\ell-1}(z), \quad z \in \mathcal{M}_N, \quad (2.3)$$

where $B_{N,\ell}$ is a user-chosen parameter, and $\mu_{N,\ell-1}$, $\sigma_{N,\ell-1}$ are the mean and standard deviation of the posterior distribution $\pi_N(\cdot | y_1, \dots, y_{\ell-1})$. Denoting by $c_N(\cdot, \cdot)$ the covariance function of the

surrogate prior π_N , i.e., $c_N(x_i, x_j)$ is the covariance between $u_N(x_i)$ and $u_N(x_j)$ for $u_N \sim \pi_N$, we have the expressions

$$\begin{aligned}\mu_{N,\ell-1}(z) &= c_{N,\ell-1}(z)^\top (C_{N,\ell-1} + \sigma^2 I)^{-1} Y_{\ell-1}, \\ \sigma_{N,\ell-1}^2(z) &= c_N(z, z) - c_{N,\ell-1}(z)^\top (C_{N,\ell-1} + \sigma^2 I)^{-1} c_{N,\ell-1}(z),\end{aligned}\quad z \in \mathcal{M}_N, \quad (2.4)$$

where $Y_{\ell-1} = (y_1, \dots, y_{\ell-1})^\top \in \mathbb{R}^{\ell-1}$, $c_{N,\ell-1}(z) \in \mathbb{R}^{\ell-1}$ is a vector with entries $(c_{N,\ell-1}(z))_i = c_N(z, z_i)$, and $C_{N,\ell-1} \in \mathbb{R}^{(\ell-1) \times (\ell-1)}$ is a matrix with entries $(C_{N,\ell-1})_{ij} = c_N(z_i, z_j)$.

Algorithm 2.1 The GGP-UCB Algorithm

Input: Point cloud \mathcal{M}_N ; prior π_N ; initialization z_0 ; total iterations L ; parameters $\{B_{N,\ell}\}_{\ell=1}^L$.

for $\ell = 1, \dots, L$ **do**

Observe $y_{\ell-1} = f(z_{\ell-1}) + \eta_{\ell-1}$.

Compute $\mu_{N,\ell-1}$ and $\sigma_{N,\ell-1}$ based on $\{(z_k, y_k)\}_{k=0}^{\ell-1}$.

Choose $z_\ell = \arg \max_{z \in \mathcal{M}_N} \left\{ \mu_{N,\ell-1}(z) + B_{N,\ell} \sigma_{N,\ell-1}(z) \right\}$.

end for

Output: z_1, \dots, z_L .

The GGP-UCB method is summarized in Algorithm 2.1. The intuition is that maximizing the acquisition function (2.3) represents a compromise between choosing points where the mean of the surrogate is large (exploitation) and where the variance is large (exploration). The parameter $B_{N,\ell}$ balances these two competing goals and its choice is crucial to the performance of the algorithm. In particular, we will discuss in Subsection 2.4 a choice of $B_{N,\ell}$ that helps correct for misspecification arising from the point cloud representation of \mathcal{M} , and we will discuss in Section 3.3 a practical approach for tuning $B_{N,\ell}$ empirically. Finally, we point out that in practice one may choose to return as output of the algorithm the candidate z_ℓ that leads to the largest observation y_ℓ when the noise is small, or, otherwise, the z_ℓ that maximizes the posterior mean at the L -th iteration, i.e., the mean $\mu_{N,L}$ of $\pi_N(\cdot | y_1, \dots, y_L)$.

2.3 Choice of Prior: Graph Gaussian Processes (GGPs)

In this subsection we discuss the construction of GGP models for f_N , the restriction of f to the x_i 's. We first give a brief overview of manifold GPs before describing GGPs.

2.3.1 Manifold GP Models

Since f is a function over \mathcal{M} , it will be useful to start by recalling the construction of GPs over \mathcal{M} . A naive approach would be to simply use geodesic distances instead of Euclidean ones in covariance functions such as the Matérn and squared exponential (SE)

$$c_{\nu,\kappa}^{\text{Ma}}(x, \tilde{x}) = \frac{2^{1-\nu}}{\Gamma(\nu)} (\kappa |x - \tilde{x}|)^\nu K_\nu(\kappa |x - \tilde{x}|), \quad c_\tau^{\text{SE}}(x, \tilde{x}) = \exp\left(-\frac{|x - \tilde{x}|^2}{4\tau}\right),$$

where $|\cdot|$ denotes the Euclidean distance, Γ is the gamma function, and K_ν is the modified Bessel function of the second kind. The parameters ν and κ in the Matérn covariance control the smoothness of sample paths and the inverse length scale of the field, while the parameter τ in the squared

exponential covariance controls the length scale. (Note that we are not including the variance parameter that usually appears as a multiplicative constant in the covariances.) Unfortunately, the naive idea of plugging in geodesic distances often leads to failure of positive definiteness of the resulting covariance matrix [28, 19].

To circumvent this challenge, the seminal paper [41] exploits the stochastic partial differential equation (SPDE) representation of Euclidean GPs with the Matérn covariance function. More precisely, it is shown in [54] that the GP with covariance function $c_{\nu, \kappa}^{\text{Ma}}$ over an Euclidean space \mathbb{R}^m is the unique stationary solution to the following equation (up to a multiplicative constant independent of κ)

$$(\kappa^2 - \Delta)^{\frac{\nu}{2} + \frac{m}{4}} u(x) = \kappa^\nu \mathcal{W}(x), \quad x \in \mathbb{R}^m, \quad (2.5)$$

where Δ is the usual Laplacian on \mathbb{R}^m and \mathcal{W} is a spatial white noise with unit variance. The equation (2.5) can then be lifted to the manifold case to construct Matérn GPs over manifolds [41]. Based on this idea, the papers [45, 6] study the following series definition of GPs over compact manifolds:

$$\text{(Matérn manifold-GP)} \quad u^{\text{Ma}} = \kappa^{s - \frac{m}{2}} \sum_{i=1}^{\infty} (\kappa^2 + \lambda_i)^{-\frac{s}{2}} \xi_i \psi_i, \quad \xi_i \stackrel{i.i.d.}{\sim} \mathcal{N}(0, 1), \quad (2.6)$$

where (λ_i, ψ_i) 's are eigenvalue-eigenfunction pairs of the negative Laplace-Beltrami operator $-\Delta_{\mathcal{M}}$ on \mathcal{M} . Compactness of \mathcal{M} ensures that $\Delta_{\mathcal{M}}$ admits a countable eigenbasis so that the solution to the analog equation of (2.5) over \mathcal{M} can be represented as the series (2.6). The parameters $s, \kappa > 0$ in (2.6) control the smoothness and the inverse length scale as in the Euclidean case: $s = \nu + m/2$ controls the spectrum decay, while κ acts as a cutoff on the essential frequencies. The scaling factor $\kappa^{s - \frac{m}{2}}$ ensures that samples from different κ 's have L^2 -norms on the same order (see. e.g. [45, Remark 2.1]), which is essential in applications where κ needs to be inferred.

As the smoothness parameter $\nu \rightarrow \infty$, it can be shown that the Matérn covariance converges (after a suitable normalization) to the SE covariance (see e.g. [55, Section 4.2]). Accordingly, there is a similar SPDE to (2.5) that characterizes the SE GP on an Euclidean space \mathbb{R}^m [6]:

$$e^{-\frac{\tau \Delta}{2}} u(x) = \tau^{\frac{m}{4}} \mathcal{W}(x), \quad x \in \mathbb{R}^m,$$

which motivates its manifold analog as the series expansion

$$\text{(SE manifold-GP)} \quad u^{\text{SE}} = \tau^{\frac{m}{4}} \sum_{i=1}^{\infty} e^{-\frac{\lambda_i \tau}{2}} \xi_i \psi_i, \quad \xi_i \stackrel{i.i.d.}{\sim} \mathcal{N}(0, 1), \quad (2.7)$$

where (λ_i, ψ_i) 's are eigenvalue-eigenfunction pairs of $-\Delta_{\mathcal{M}}$. Here the factor $\tau^{\frac{m}{4}}$ is again interpreted as balancing the magnitude of samples from different τ 's (see Lemma A.4). Furthermore, the induced covariance function has the form

$$c^{\text{SE}}(x, \tilde{x}) = \tau^{\frac{m}{2}} \sum_{i=1}^{\infty} e^{-\lambda_i \tau} \psi_i(x) \psi_i(\tilde{x}). \quad (2.8)$$

Notice that this is also known as the heat kernel (up to the scaling factor $\tau^{m/2}$), which is a natural generalization of the SE kernel over the manifold. A similar expression holds for the induced covariance function of u^{Ma} :

$$c^{\text{Ma}}(x, \tilde{x}) = \kappa^{2s-m} \sum_{i=1}^{\infty} (\kappa^2 + \lambda_i)^{-s} \psi_i(x) \psi_i(\tilde{x}). \quad (2.9)$$

Besides the connection with their Euclidean counterparts, notice that the random fields (2.6) and (2.7) are series expansions of the eigenfunctions of the Laplace-Beltrami operator, which form an orthonormal basis for $L^2(\mathcal{M})$ and carry rich information about the geometry of \mathcal{M} ; therefore, (2.6) and (2.7) are natural GP models for functions over \mathcal{M} . However, computing the pairwise covariances (2.8) and (2.9) between any two points would require knowledge of the Laplace-Beltrami eigenvalues and eigenfunctions, which are only known analytically for a few manifolds such as the sphere and the torus, and can otherwise be expensive to approximate. More importantly, in applications where only a point cloud representation of \mathcal{M} is available we need an empirical way to approximate the manifold GPs (2.6) and (2.7). To that end, we will adopt a manifold learning approach using graph Laplacians.

2.3.2 GGP Models

Given a point cloud $\mathcal{M}_N = \{x_1, \dots, x_N\} \subset \mathcal{M}$, recall that our goal is to build a GP model for f_N , the restriction of f to the x_i 's. It then suffices to construct an N -dimensional Gaussian that approximates the manifold GPs (2.6) and (2.7); in particular, we need to construct a suitable covariance matrix.

To start with, observe that the manifold Matérn GP (2.6) can be seen as the Karhunen-Loève expansion of the Gaussian measure [3] (the infinite-dimensional analog of multivariate Gaussian) $\mathcal{N}(0, \mathcal{C})$, where \mathcal{C} is the covariance operator

$$\mathcal{C} = \kappa^{2s-m} (\kappa^2 I - \Delta_{\mathcal{M}})^{-s},$$

with I denoting the identity operator. Therefore a natural candidate for an N -dimensional approximation is to consider the multivariate Gaussian $\mathcal{N}(0, \mathcal{C}_N)$, where

$$\mathcal{C}_N = \kappa^{2s-m} (\kappa^2 I_N + \Delta_N)^{-s} \quad (2.10)$$

for some $\Delta_N \in \mathbb{R}^{N \times N}$ constructed with the x_i 's that approximates $-\Delta_{\mathcal{M}}$ with I_N denoting the N -dimensional identity matrix. We shall set Δ_N to be a suitable *graph Laplacian*, as we describe next.

Let $\mathcal{M}_N = \{x_i\}_{i=1}^N$ be a collection of points on \mathcal{M} . One can construct a weighted graph over the x_i 's by introducing a weight matrix $W \in \mathbb{R}^{N \times N}$ whose entry W_{ij} represents the similarity between points x_i and x_j . The *unnormalized graph Laplacian* is then defined as $\Delta_N = D - W$, where D is a diagonal matrix whose entries are $D_{ii} = \sum_{j=1}^N W_{ij}$. One can immediately check that Δ_N is symmetric and positive semi-definite using the relation

$$v^\top \Delta_N v = \frac{1}{2} \sum_{i=1}^N \sum_{j=1}^N W_{ij} |v_i - v_j|^2, \quad v \in \mathbb{R}^N,$$

implying that Δ_N admits a spectral decomposition with nonnegative eigenvalues $\{\lambda_{N,i}\}_{i=1}^N$ (ordered increasingly) and the associated eigenvectors $\{\psi_{N,i}\}_{i=1}^N$ form an orthonormal basis for \mathbb{R}^N . Several normalizations of Δ_N have also been considered, including the *random walk graph Laplacian* $\Delta_N^{\text{rw}} = D^{-1}\Delta_N$ and *symmetric graph Laplacian* $\Delta_N^{\text{sym}} = D^{-1/2}\Delta_N D^{-1/2}$, see [53]. We focus on the unnormalized version due to its symmetry, which makes it a valid choice in the covariance matrix (2.10), and its convergence properties that we will describe now.

As its name suggests, Δ_N approximates, in a suitable sense, the Laplace-Beltrami operator. Indeed, if we set the pairwise similarity to be

$$W_{ij} = \frac{2(m+2)}{N\nu_m h_N^{m+2}} \mathbf{1}\{|x_i - x_j| < h_N\}, \quad (2.11)$$

where $|\cdot|$ denotes the Euclidean distance, ν_m is the volume of the m -dimensional unit ball and h_N is a graph connectivity parameter, then for suitable choices of h_N it can be shown (see e.g. [25] or Proposition A.2) that the eigenpair $(\lambda_{N,i}, \psi_{N,i})$ of Δ_N approximates the corresponding eigenpair (λ_i, ψ_i) of $-\text{vol}(\mathcal{M})^{-1}\Delta_{\mathcal{M}}$. Based on this fact, we shall now define two GGP's as follows

$$\text{(Matérn GGP)} \quad u_N^{\text{Ma}} = \kappa^{s-\frac{m}{2}} \sum_{i=1}^{k_N} (\kappa^2 + \lambda_{N,i})^{-\frac{s}{2}} \xi_i \psi_{N,i}, \quad \xi_i \stackrel{i.i.d.}{\sim} \mathcal{N}(0, 1), \quad (2.12)$$

$$\text{(SE GGP)} \quad u_N^{\text{SE}} = \tau^{\frac{m}{4}} \sum_{i=1}^{k_N} e^{-\frac{\lambda_{N,i}\tau}{2}} \xi_i \psi_{N,i}, \quad \xi_i \stackrel{i.i.d.}{\sim} \mathcal{N}(0, 1), \quad (2.13)$$

where $k_N \leq N$ is a truncation level to be determined. Notice that Matérn and SE GGP's can be interpreted as discretely indexed GPs over the graph (\mathcal{M}_N, W) , hence the name GGP. Similar objects have also been studied by [45, 7, 17]. When $k_N = N$, we see that (2.12) is nothing but the multivariate Gaussian $\mathcal{N}(0, \kappa^{2s-m}(\kappa^2 I_N + \Delta_N)^{-s})$, matching our goal (2.10) at the beginning. The motivation for introducing the truncation is that the spectral approximation accuracy degrades quickly when we go to higher modes (see e.g. Proposition A.2), where the error bounds are only meaningful when $h_N \sqrt{\lambda_i} \ll 1$. Therefore (2.12) can be seen as a low rank approximation of (2.10) that keeps only the low and accurate frequencies. By Weyl's law (see e.g. [11, Theorem 72]), $\lambda_i \asymp i^{2/m}$ and in particular $\lambda_i \rightarrow \infty$, which suggests a necessary condition $k_N \ll h_N^{-m}$. In Subsection 3.2 we discuss an empirical way of choosing k_N . The induced covariance functions take the form

$$\begin{aligned} c_N^{\text{Ma}}(x, \tilde{x}) &= \kappa^{2s-m} \sum_{i=1}^{k_N} (\kappa^2 + \lambda_{N,i})^{-s} \psi_{N,i}(x) \psi_{N,i}(\tilde{x}), \\ c_N^{\text{SE}}(x, \tilde{x}) &= \tau^{\frac{m}{2}} \sum_{i=1}^{k_N} e^{-\lambda_{N,i}\tau} \psi_{N,i}(x) \psi_{N,i}(\tilde{x}), \end{aligned} \quad x, \tilde{x} \in \mathcal{M}_N. \quad (2.14)$$

Notice that the definitions (2.12) and (2.13) are completely parallel with (2.6) and (2.7); hence the spectral convergence of Δ_N leads to convergence of GGP's to their manifold counterparts. We will rely on the following assumption:

Assumption 2.2. \mathcal{M} is a smooth, compact and connected submanifold of dimension $m \geq 2$ in \mathbb{R}^d that has no boundary and bounded sectional curvature, normalized so that $\text{vol}(\mathcal{M}) = 1$. Assume the x_i 's are i.i.d. samples from the uniform distribution on \mathcal{M} .

The following result provides a simplified statement of the convergence analysis for Matérn GGPs in [45, 46] and in addition covers SE GGPs.

Proposition 2.3. *Let $0 < \iota < 1$ be arbitrary. Define $\alpha_m = (m + 4 + \iota) \vee (2m)$ and $\beta_{m,s} = \frac{2s-3m+1}{6m+6} \wedge 1$. Let $p_m = \frac{3}{4}$ when $m = 2$ and $p_m = \frac{1}{m}$ otherwise. For $s > \frac{3}{2}m - \frac{1}{2}$, set*

$$\begin{aligned} \text{(Matérn GGP)} \quad h_N &\asymp N^{-\frac{1}{\alpha_m}} (\log N)^{\frac{p_m}{2}}, \quad k_N \asymp N^{\frac{m\beta_{m,s}}{(2s-3m+1)\alpha_m}} (\log N)^{-\frac{mp_m\beta_{m,s}}{(4s-6m+2)}}, \\ \text{(SE GGP)} \quad h_N &\asymp N^{-\frac{1}{\alpha_m}} (\log N)^{\frac{p_m}{2}}, \quad (\log N)^{\frac{m}{2}} \ll k_N \ll N^{\frac{m}{(3m+3)\alpha_m}} (\log N)^{-\frac{mp_m}{6m+6}}. \end{aligned}$$

Under Assumption 2.2, with probability $1 - O(N^{-c})$ for some $c > 0$, there exists $T_N : \mathcal{M} \rightarrow \{x_1, \dots, x_N\}$ satisfying $T_N(x_i) = x_i$ such that

$$\left. \begin{aligned} \mathbb{E} \|u_N^{Ma} \circ T_N - u^{Ma}\|_\infty &\lesssim N^{-\frac{\beta_{m,s}}{2\alpha_m}} (\log N)^{\frac{\beta_{m,s} p_m}{4}} \\ \mathbb{E} \|u_N^{SE} \circ T_N - u^{SE}\|_\infty &\lesssim N^{-\frac{1}{2\alpha_m}} (\log N)^{\frac{p_m}{4}} \end{aligned} \right\} =: \epsilon_N. \quad (2.15)$$

The fact that we can study L^∞ -norms of these random fields follows from their almost sure continuity established in [46, Lemma 3] and Lemma A.4 below. Proposition 2.3 will be a key ingredient in establishing regret bounds for GGP-UCB.

2.4 Choice of Acquisition Function

When the GGP prior π_N matches the truth f_N , i.e., when f_N is a sample from π_N , [49] gives a choice of $B_{N,L}$ for the acquisition function (2.3) that ensures vanishing regret. However, this is not necessarily true in our case since f_N is the restriction of a continuum function f over \mathcal{M} whereas the GGP π_N is only constructed with \mathcal{M}_N . A mismatch is possible and below we address this issue following ideas in [4].

Suppose that the function f to be optimized is a sample from the manifold GP (2.6) (or (2.7)) and we adopt the corresponding GGP prior π_N given by (2.12) (resp. (2.13)) for f_N . Proposition 2.3 then implies that if $u_N \sim \pi_N$, we have with probability $1 - \delta$

$$\|u_N - f_N\|_\infty \leq \delta^{-1} \epsilon_N, \quad (2.16)$$

where here $\|\cdot\|_\infty$ denotes the entry-wise maximum and ϵ_N is a placeholder for the approximation error defined in (2.15). In other words, there is potentially a *misspecification error* coming from the fact that we are using an approximate GP to model f_N . With the understanding of such error obtained in Proposition 2.3, we can follow the approach in [4] and set

$$B_{N,\ell} = \sqrt{2 \log \left(\frac{\pi^2 \ell^2 N}{6\delta} \right)} + \frac{\epsilon_N \sqrt{\ell - 1}}{\delta \sigma}, \quad (2.17)$$

where we recall that σ is the noise standard deviation. Notice that this differs from the plain GP-UCB in [49] by the additional term $\epsilon_N \sqrt{\ell - 1} / \delta \sigma$ that aims to correct for the misspecification. Intuitively, such correction leads to an increase of the weight on the posterior standard deviation, which accounts for the increased uncertainty due to the approximate modeling. Therefore at the ℓ -th iteration, we shall pick the candidate z_ℓ as

$$z_\ell = \arg \max_{z \in \mathcal{M}_N} \left\{ \mu_{N,\ell-1}(z) + \left[\sqrt{2 \log \left(\frac{\pi^2 \ell^2 N}{6\delta} \right)} + \frac{\epsilon_N \sqrt{\ell - 1}}{\delta \sigma} \right] \sigma_{N,\ell-1}(z) \right\}, \quad (2.18)$$

where $\mu_{N,\ell-1}$ and $\sigma_{N,\ell-1}$ are defined as in (2.4) but with $c_N(\cdot, \cdot)$ being the graph covariance functions (2.14).

2.5 Main Result: Regret Bounds

Now we are ready to state our main result.

Theorem 2.4. *Suppose f is a sample from the Matérn manifold-GP (2.6) with parameters κ, s (resp. SE manifold-GP (2.7) with parameter τ). Let π_N be the Matérn (resp. SE) GGP constructed as in Proposition 2.3 with the same parameters. Apply Algorithm 2.1 with π_N and with $B_{N,\ell}$ given by (2.17). Under Assumption 2.2, for N large enough, we have with probability $1 - 2\delta - O(N^{-c})$ that*

$$r_{N,L} \leq C \left[\frac{\sqrt{2 \log(\pi^2 L^2 N / 6\delta)}}{\sqrt{L}} + \frac{\epsilon_N}{\delta\sigma} \right] \sqrt{k_N \log L}, \quad \forall L \geq 1,$$

where $c, C > 0$ are universal constants. Here we recall that σ is the observation noise standard deviation, k_N is the truncation parameter in Proposition 2.3, and ϵ_N is the approximation error as in (2.15).

Remark 2.5. By plugging the scaling in Proposition 2.3, we get

$$r_{N,L} = \tilde{O}\left((L^{-\frac{1}{2}} + \epsilon_N)\sqrt{k_N}\right) = \tilde{O} \begin{cases} L^{-\frac{1}{2}} N^{\frac{m\beta_{m,s}}{(4s-6m+2)\alpha_m}} + N^{-\frac{(4s-7m+2)\beta_{m,s}}{(4s-6m+2)\alpha_m}} & \text{(Matérn)} \\ L^{-\frac{1}{2}} + N^{-\frac{1}{2\alpha_m}} & \text{(SE)} \end{cases}.$$

Here the notation $\tilde{O}(\cdot)$ means that we have dropped all dependence on logarithmic factors. The regret goes to zero as both N and L approach infinity in both cases (when $s > \frac{7}{4}m + \frac{1}{2}$ for the Matérn case), although we recall that N should be treated as a fixed large number and L is the running index. The two terms in the above upper bound can be understood as the error incurred by Bayesian optimization and by misspecification, respectively. For a fixed N , the regret will decrease as $L \rightarrow \infty$ to a threshold imposed by the misspecification error, which itself will go to zero with more data points from \mathcal{M} as $N \rightarrow \infty$. Notice that the two terms are balanced at $L \asymp N^{\beta_{m,s}/\alpha_m}$ for the Matérn case and $L \asymp N^{1/\alpha_m}$ for the SE case. Since $\beta_{m,s} \leq 1$, for a fixed large enough N , number of queries of the order $L \ll N$ would be sufficient in both cases because otherwise the error coming from misspecification will dominate. We shall demonstrate by simulations in Section 4 that the algorithm is able to find the optimizer (or an almost optimizer) after a number L of queries that is significantly smaller than the size N of the point cloud. \square

3 Estimation and Tuning of GGP-UCB Parameters

This section discusses important considerations for the practical implementation of the GGP-UCB algorithm. Subsections 3.1, 3.2 and 3.3 describe respectively the estimation of prior GGP parameters, the choice of graph connectivity h_N and truncation level k_N , and the empirical tuning of the acquisition function.

3.1 Parameter Estimation

Theorem 2.4 holds under the assumption that the GGP model uses the same parameters κ, s, τ as those for the truth. However, these parameters are typically unavailable in practice and need to be estimated. In this subsection we give a possible empirical solution.

Recall that at the ℓ -th iteration we pick the next query point z_ℓ based on (2.18) and observe a noisy function value

$$y_\ell = f(z_\ell) + \eta_\ell,$$

where f is assumed to be a sample from the manifold GP (2.6) or (2.7) with parameter θ ($\theta = (\kappa, s)$ for the Matérn case and $\theta = \tau$ for the SE case). We shall obtain an estimate θ_ℓ of θ in each iteration of the above procedure using a maximum likelihood estimation approach:

$$\theta_\ell = \arg \max_{\theta} \mathbb{P}(Y_\ell | \theta), \quad (3.1)$$

where $Y_\ell = (y_1, \dots, y_\ell)^\top$. Exact maximization of (3.1) would require knowing the covariance structure of the underlying manifold GP, in particular the eigenpairs of the Laplace-Beltrami operator, the lack of which is precisely the reason why we introduced our graph-based approach. However, since the GGPs (2.12) and (2.13) are what we actually use for modeling f , a natural idea is then to seek for parameters of these surrogate models that can best fit the data. Therefore we shall consider the following “surrogate” data model by pretending that the y_ℓ ’s are generated from the GGPs:

$$\begin{aligned} y_k &= u_N(z_k) + \eta_k, & \eta_k &\stackrel{i.i.d.}{\sim} \mathcal{N}(0, \sigma^2), & k &= 1, \dots, \ell, \\ u_N &\sim \mathcal{N}(0, \mathcal{C}_N^\theta), \end{aligned}$$

where \mathcal{C}_N^θ is the covariance matrix associated with (2.14). It follows that

$$Y_\ell \sim \mathcal{N}(0, \Sigma_N^\theta), \quad \Sigma_N^\theta = A \mathcal{C}_N^\theta A^\top + \sigma^2 I_\ell, \quad (3.2)$$

where $A \in \mathbb{R}^{\ell \times N}$ is a matrix of 0’s and 1’s whose entries indicate the indices of the z_ℓ ’s among $\mathcal{M}_N = \{x_i\}_{i=1}^N$. Maximization of the likelihood of Y_ℓ under (3.2) gives the estimate θ_ℓ .

3.2 Determining the Truncation Level k_N and the Graph Connectivity h_N

As mentioned in Subsection 2.3.2, the truncation level k_N is crucial in that the higher frequencies obtained from the graph Laplacian give poor approximations to their manifold counterparts and can have a negative impact on approximating manifold GPs. Proposition 2.3 gives a scaling for k_N that is based on the asymptotic behavior of the graph Laplacian. Empirically, one can simply choose k_N by plotting the spectrum of Δ_N .

Proposition A.2 in the appendix gives an upper bound on the eigenvalue approximation, where the error is small only when $h_N \sqrt{\lambda_i} \ll 1$. In practice, what we usually observe is not only such poor spectral approximation for large i ’s, but also a “saturation” of the graph Laplacian eigenvalues after certain threshold. Figure 1 shows the first several eigenvalues of the Laplace-Beltrami operator $-\Delta_{\mathcal{M}}$ and the graph Laplacian Δ_N constructed with (a) $N = 500$ points from the unit circle; and (b) $N = 3000$ points from the unit sphere. We can see from both plots that for small index i , the eigenvalues $\lambda_{N,i}$ of Δ_N approximate well the eigenvalues λ_i of $-\Delta_{\mathcal{M}}$; however, the spectrum of Δ_N is essentially flat for large i . Therefore one can choose k_N to be around the point of saturation in the spectrum of Δ_N . Such saturation phenomenon, noted for instance in [26, 23, 24], also helps to explain the need for truncation. Indeed, the eigenvalues $\lambda_{N,i}$ determine the decay of the coefficients

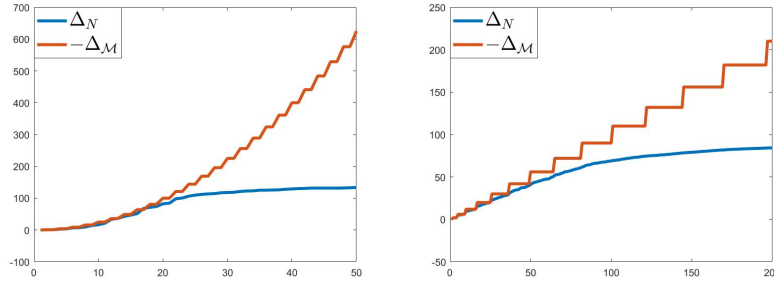


Figure 1 Spectrum of Δ_N versus spectrum of $-\Delta_{\mathcal{M}}$ for the unit circle (left) and the unit sphere (right).

in the series (2.12) and (2.13) defining our GGPs. Without a truncation, too much weight would be given to the high frequencies, which would lead to overly rough sample paths.

Another key parameter in the construction of our GGPs is the graph connectivity h_N in the definition of the weights (2.11). A common choice [25, 46] is $h_N \propto \sqrt{\rho_N}$, where ρ_N defined in (A.1) can be interpreted as the maximum distance between any two nearby x_i 's or the “resolution” of \mathcal{M}_N . In particular, the choice $h_N \propto \sqrt{\rho_N}$ ensures that the neighborhood of each x_i in the graph is local but rich enough to capture the local geometry. Moreover, this choice balances the two terms in the error bound $\rho_N/h_N + h_N\sqrt{\lambda_i}$ in Proposition A.2. The scaling of ρ_N is shown in [25, Theorem 2] and recorded in Proposition A.1, which leads to the choice $h_N = CN^{-1/2m}$ (the logarithmic factor can be absorbed into the proportion constant). The proportion constant can be determined again by plotting the corresponding spectrum of Δ_N . Starting with a large C , one can keep decreasing the value of C while observing the point of saturation becoming larger, until one hits a point where the spectrum is no longer meaningful. This latter case will happen when h_N is too small so that the graph is disconnected and the graph Laplacian has repeated zero eigenvalues.

3.3 Empirical Tuning of the Acquisition Function

Recall that the selection rule (2.18) incorporates information on the level of misspecification ϵ_N incurred by the GGPs. Proposition 2.3 gives such a bound on ϵ_N , which goes to zero as $N \rightarrow \infty$. However, for practical considerations, the upper bound may not be small for certain ranges of δ and N , especially since there is a possibly non-sharp proportion constant in ϵ_N . Therefore this could cause the term $\epsilon_N\sqrt{\ell-1}/\delta\sigma$ in $B_{N,\ell}$ to be overly large, so that the acquisition function puts too much weight on the posterior standard deviation, as a result of which exploration overwhelms exploitation. For this reason, we shall consider instead setting $B_{N,\ell}$ as

$$B_{N,\ell} = a \sqrt{2 \log \left(\frac{\pi^2 \ell^2 N}{6\delta} \right)}, \quad (3.3)$$

with a tuning parameter $a > 0$. As noticed in the simulation studies in [49], setting $a = 1/5$ in practice leads to the best performance in well-specified cases, i.e., when $\epsilon_N = 0$ (although their theoretical results are proved for $a = 1$). Motivated by this observation, we shall set $a = 1/2$ throughout for our simulation studies in Section 4 to account for the case $\epsilon_N \neq 0$. The idea is that the original correction term $\epsilon_N\sqrt{\ell-1}/\delta\sigma$ for misspecification is now absorbed as the increment $(1/2 - 1/5)\sqrt{2 \log(\pi^2 \ell^2 N/6\delta)}$.

Finally, the selection rule (2.18) searches for the query points over the entire \mathcal{M}_N at each iteration, which could return points that have already been picked and get stuck at local optima in practice. We shall modify (2.18) slightly by maximizing it over $\mathcal{M}_N \setminus \{z_1, \dots, z_{\ell-1}\}$ at the ℓ -th iteration, i.e., by asking the algorithm to output a query point that has not been chosen in previous iterations.

4 Numerical Examples

This section contains numerical experiments that complement the theory and illustrate the performance of our method. In Subsection 4.1 we give a detailed investigation of our approach over the unit circle, including the parameter estimation technique discussed in Subsection 3.1. In Subsections 4.2 and 4.3 we consider artificial manifolds for which the spectrum of their Laplace-Beltrami operator is not available. Finally, in Subsection 4.4 we consider a heat source detection problem over the sphere as an application in inverse problems.

Throughout all the examples in Subsections 4.1-4.3, we set $\sigma = 0.05 \cdot \|f_N\|_2 / \sqrt{N}$, which corresponds to a noise level of roughly 5%. We adopt the selection rule (3.3) and set $\delta = 0.1$ in the choice of $B_{N,\ell}$.

4.1 Parameter Estimation and Truncation Level on the Unit Circle

Let \mathcal{M} be the unit circle in \mathbb{R}^2 and $\{x_i\}_{i=1}^{N=500}$ be i.i.d. samples from the uniform distribution over \mathcal{M} . Since the eigenvalues and eigenfunctions of the Laplace-Beltrami operator on the unit circle are available in closed form, here we are able to generate the truth by sampling the manifold GPs (2.6) and (2.7); this enables us to clearly illustrate the effects of truncation and parameter estimation in our algorithm.

To start with, suppose first that f is a sample from the manifold Matérn GP (2.6) with parameters τ_* and s_* , which can be generated from (2.6) with a sufficiently high truncation. We shall compare the performance of Algorithm 2.1 with different choices of the prior. Specifically, consider

$$\text{(GGP-UCB)} \quad u^{\text{Full}} = \kappa_*^{s_* - \frac{m}{2}} \sum_{i=1}^N (\kappa_*^2 + \lambda_{N,i})^{-\frac{s_*}{2}} \xi_i \psi_{N,i}, \quad \xi_i \stackrel{i.i.d.}{\sim} \mathcal{N}(0, 1), \quad (4.1)$$

$$\text{(GGP-UCB-T)} \quad u^{\text{Trun}} = \kappa_*^{s_* - \frac{m}{2}} \sum_{i=1}^{k_N} (\kappa_*^2 + \lambda_{N,i})^{-\frac{s_*}{2}} \xi_i \psi_{N,i}, \quad \xi_i \stackrel{i.i.d.}{\sim} \mathcal{N}(0, 1), \quad (4.2)$$

$$\text{(GGP-UCB-ML)} \quad u^{\text{MLE}} = \kappa_\ell^{s_\ell - \frac{m}{2}} \sum_{i=1}^{k_N} (\kappa_\ell^2 + \lambda_{N,i})^{-\frac{s_\ell}{2}} \xi_i \psi_{N,i}, \quad \xi_i \stackrel{i.i.d.}{\sim} \mathcal{N}(0, 1), \quad (4.3)$$

where κ_ℓ and s_ℓ are the estimated parameters as discussed in Subsection 3.1. Notice that (4.2) is the same as (2.13) with true parameters κ_*, s_* . The model (4.1) is a variant without truncation, whereas (4.3) is a variant that uses estimated parameters. We set $k_N = 20$ and $h_N = 4 \times N^{-1/2}$ in the construction of Δ_N .

Remark 4.1. Joint estimation of κ_ℓ, s_ℓ for (4.3) turns out to be unstable, partly due to the fact that not all parameters for the Matérn model are identifiable (see e.g. [58, 5, 40]) and limited understanding of the associated maximum likelihood estimators. Therefore in the simulations below, we fix κ_ℓ to be 1 throughout and only estimate s_ℓ . The choice of κ_ℓ is motivated by our empirical

observation that a smaller κ_ℓ than the true one gives better performance. We hope to investigate such phenomenon and in general maximum likelihood estimation over graph-based surrogate models in the future. \square

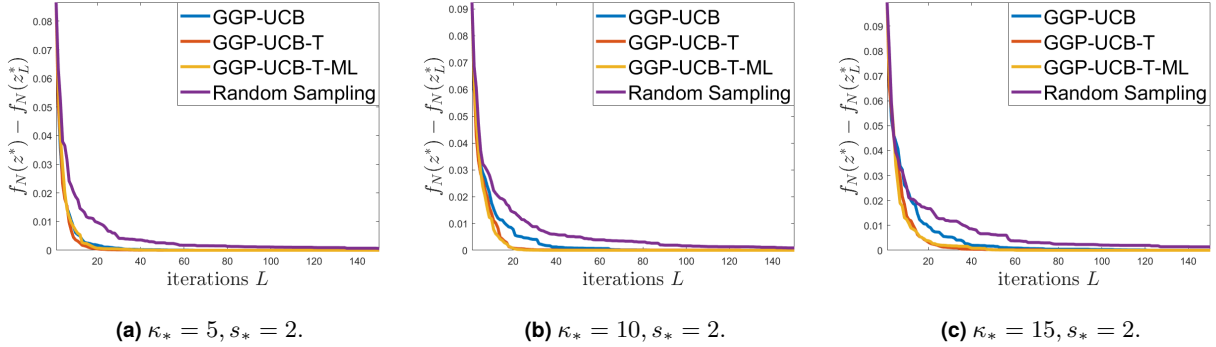


Figure 2 Comparisons of the simple regrets obtained from GGP-UCB (prior with (4.1)), GGP-UCB-T (prior with (4.2)), GGP-UCB-T-ML (prior with (4.3)), and random sampling when f is a Matérn GP (2.6). The results are averaged over 50 trials.

Figure 2 shows the comparison for three sets of parameters (κ_*, s_*) . In all cases, the two approaches with truncated prior modeling lead to the smallest regret and find the maximum in less than $L = 50$ iterations, which is much smaller than the size $N = 500$ in the point cloud. Incorporating maximum likelihood estimation of the parameters gives competitive performance compared to the case when the parameters are assumed to be known. Finally, all graph-based algorithms clearly outperform random sampling (picking a new query point uniformly randomly at each iteration), which we include as a baseline. In a parallel setting, we also perform a similar comparison when the truth is a SE GP (2.7), where the graph SE GP (2.13) is used for modeling. Note that in this case there is only one parameter τ to be estimated. Figure 3 shows the comparison, which is qualitatively similar to the Matérn case.

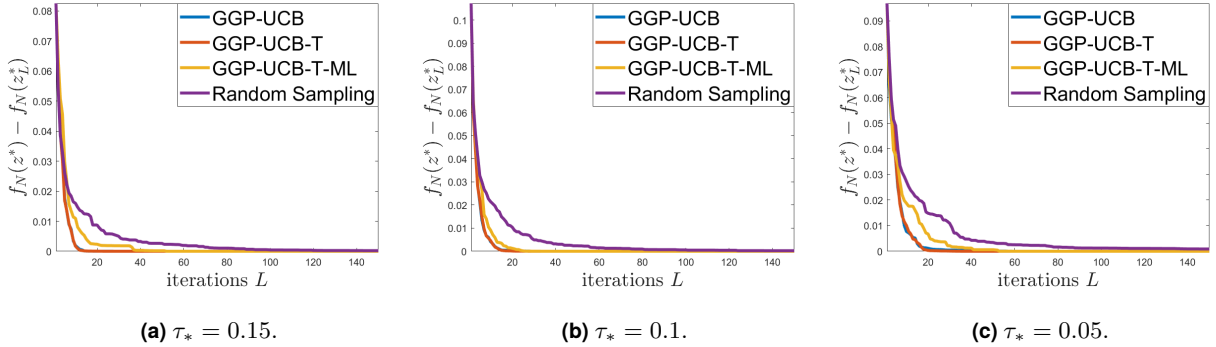


Figure 3 Comparisons of the simple regrets obtained from GGP-UCB, GGP-UCB-T, GGP-UCB-T-ML, and random sampling when f is a SE GP (2.7). The results are averaged over 50 trials.

4.2 One-Dimensional Artificial Manifold

In this subsection we consider an artificial one-dimensional manifold, whose point cloud representation is shown in Figure 4a. This example is motivated by an application to determine the busiest portion of a highway, as in [49]. Here building a GP model over the point cloud using Euclidean distances would be undesirable since, for instance, the two points marked in red are far along the manifold while being close in Euclidean sense. This motivates the use of our graph-based approach, which naturally imposes smoothness of prior draws along the hidden manifold, see Figure 4b.

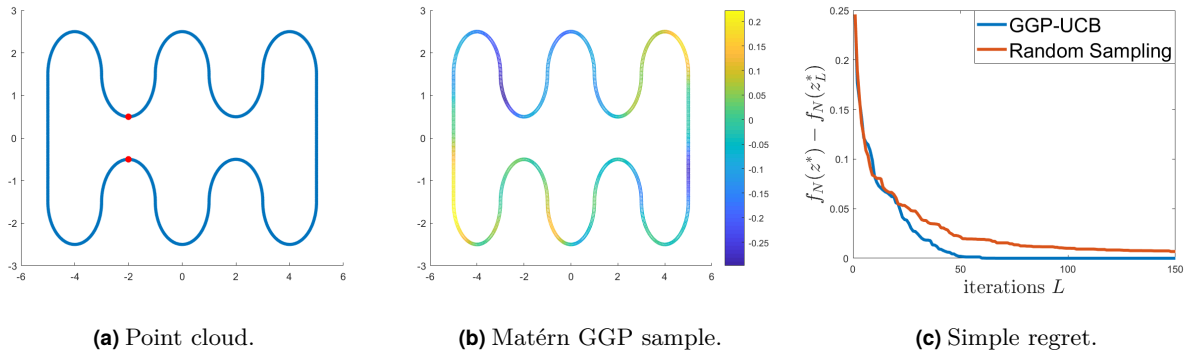


Figure 4 (a) Point cloud \mathcal{M}_N : the points in red are close in Euclidean sense but far along \mathcal{M} . (b) A random sample $u_{\bar{N}} \sim \mathcal{N}(0, \kappa_*^{2s_*-m} (\kappa_*^2 I_{\bar{N}} + \Delta_{\bar{N}})^{-s_*})$ with $\kappa_* = 1, s_* = 4$; values of $u_{\bar{N}}$ vary smoothly along \mathcal{M} . (c) Comparison of simple regrets as a function of L between GGP-UCB and random sampling. The results are averaged over 50 trials.

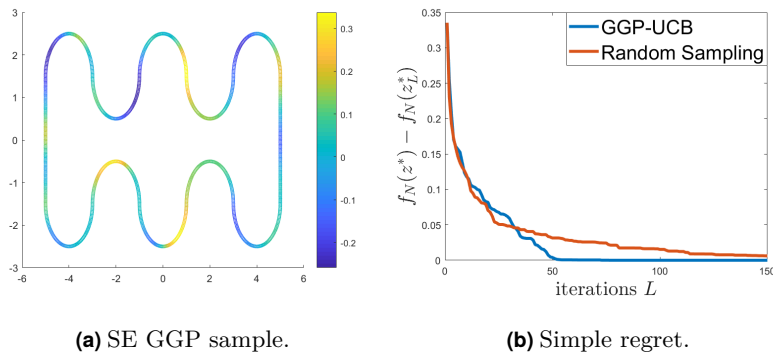


Figure 5 (a) A random sample from $\mathcal{N}(0, \tau_*^{m/2} e^{-\tau_* \Delta_{\bar{N}}})$ with $\tau_* = 2$. (b) Comparison of simple regrets as a function of L between GGP-UCB and random sampling. The results are averaged over 50 trials.

Unlike the unit circle case in Subsection 4.1, the eigenvalues and eigenfunctions of the Laplace-Beltrami operator over this new manifold are no longer known analytically. This prevents us from generating random functions from the manifold GP and we instead generate our truth from a finer point cloud than the one used for optimization. More precisely, let f be a sample from $\mathcal{N}(0, \kappa_*^{2s_*-m} (\kappa_*^2 I_{\bar{N}} + \Delta_{\bar{N}})^{-s_*})$ (cf. the full series expansion (4.1)) where $\Delta_{\bar{N}}$ is constructed with $\bar{N} = 1200$ points. We take f as our truth and subsample a point cloud of $N = 600$ points as

our \mathcal{M}_N over which we solve the optimization problem. Figure 4b shows a random sample with $\kappa_* = 1, s_* = 4$, which has several local optima. Notice that points receive a similar value if they are close along the manifold instead of in Euclidean distance. Since the main focus of this example is on the geometry, we simply adopt the full prior $\mathcal{N}(0, \kappa_*^{2s_*-m}(\kappa_*^2 I_N + \Delta_N)^{-s_*})$ constructed with \mathcal{M}_N with the same parameters κ_*, s_* as the truth are used. The graph connectivities for $\Delta_{\bar{N}}$ and Δ_N are taken as $h_{\bar{N}} = 4 \times \bar{N}^{-1/2}$ and $h_N = 4 \times N^{-1/2}$ respectively. Figure 4c compares the performance of GGP-UCB with random sampling. Note that GGP-UCB finds the optimizer in $L = 50$ iterations, which is again much smaller than the total number $N = 600$ of points in \mathcal{M}_N . Similar results are obtained for the full expansion version of SE GP (2.13), i.e., $\mathcal{N}(0, \tau_*^{m/2} e^{-\tau_* \Delta_{\bar{N}}})$, with $\tau_* = 2$ in Figure 5.

4.3 Two-Dimensional Artificial Manifold

Here we consider a two-dimensional manifold whose point cloud representation —taken from Keenan Crane’s 3D repository [13]— is shown in Figure 6a. This example is motivated by an application in finding the point of highest temperature over a surface where an explicit parameterization is not given. The point cloud consists of $\bar{N} = 2930$ data points. As in Subsection 4.2, manifold GPs are not available, so we generate the truth with all $\bar{N} = 2930$ points, but solve the optimization with a subset of $N = 1500$ points. Again, we shall focus on the untruncated prior (4.1) (and its SE version), and use the same parameters in our algorithm as the truth. The graph connectivities for $\Delta_{\bar{N}}$ and Δ_N are taken as $h_{\bar{N}} = 2 \times \bar{N}^{-1/4}$ and $h_N = 2 \times N^{-1/2}$ respectively. Figure 6a shows a sample from $\mathcal{N}(0, \kappa_*^{2s_*-m}(\kappa_*^2 I_{\bar{N}} + \Delta_{\bar{N}})^{-s_*})$ with $\kappa_* = 1, s_* = 3$. Figure 6b compares the performance of GGP-UCB with random sampling. As in previous examples, the number L of queries needed by GGP-UCB to find the optimizer is significantly smaller than the size N of the point cloud. Figures 7a and 7b show the results for the SE case with $\tau_* = 0.1$.

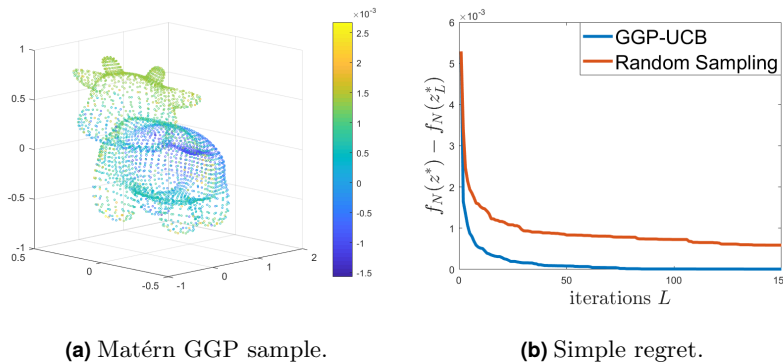


Figure 6 (a) A random sample from $\mathcal{N}(0, \kappa_*^{2s_*-m}(\kappa_*^2 I_{\bar{N}} + \Delta_{\bar{N}})^{-s_*})$ with $\kappa_* = 1, s_* = 3$. (b) Comparison of simple regrets as a function of L between GGP-UCB and random sampling. The results are averaged over 50 trials.

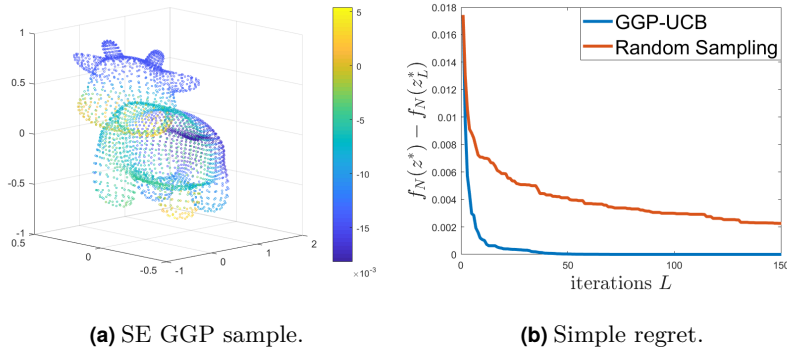


Figure 7 (a) A random sample from $\mathcal{N}(0, \tau_*^{m/2} e^{-\tau_* \Delta_N})$ with $\tau_* = 0.1$. (b) Comparison of simple regrets as a function of L between GGP-UCB and random sampling. The results are averaged over 50 trials.

4.4 Source Detection on the Sphere

In this subsection we employ our GGP-UCB method on a heat source location problem on the two-dimensional unit sphere S^2 . Consider the heat equation

$$\begin{cases} \phi_t = \Delta_{S^2} \phi, & (x, t) \in S^2 \times [0, \infty), \\ \phi(x, 0) = \phi_0(x), & x \in S^2, \end{cases} \quad (4.4)$$

where Δ_{S^2} is the Laplace-Beltrami operator on S^2 and ϕ_0 is an initial heat configuration. The solution of the heat equation for some time $t > 0$ is given by

$$\phi(x, t) = \sum_{i=1}^{\infty} \langle \phi_0, \psi_i \rangle_{S^2} \cdot e^{-\lambda_i t} \psi_i(x), \quad x \in S^2, \quad (4.5)$$

where $\{(\lambda_i, \psi_i)\}_{i=1}^{\infty}$ are the eigenpairs of $-\Delta_{S^2}$ and $\langle \cdot, \cdot \rangle_{S^2}$ is the Riemannian inner product associated to S^2 . The initial heat configuration is given by

$$\phi_0(x) = \exp(\zeta z^*{}^\top x), \quad \zeta > 0, \quad x \in S^2,$$

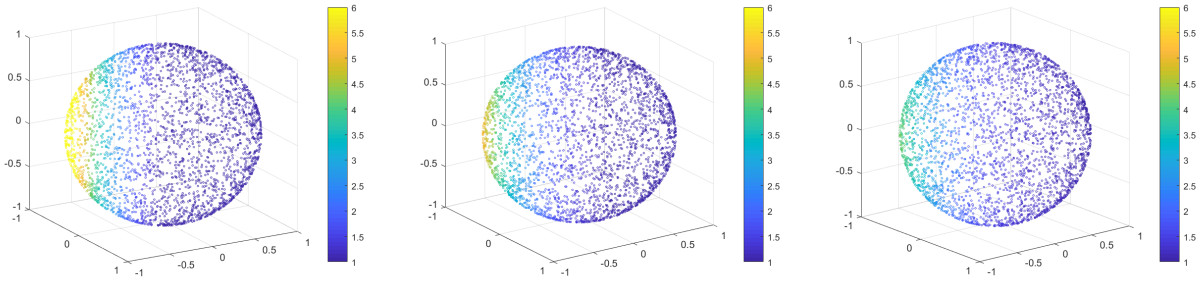
which can be viewed as an unnormalized density of the von-Mises Fisher distribution [20] on S^2 . A larger concentration parameter ζ leads to more probability mass centered around its mean z^* .

Our goal is to recover the center z^* of the initial heat configuration, assuming we are only given a point cloud $\mathcal{M}_N = \{x_i\}_{i=1}^{N=3000}$ but not \mathcal{M} directly, and noisy heat measurements at some positive time t of the form

$$\mathbf{d} = \phi(\mathbf{x}) + \eta, \quad \phi(\mathbf{x}) = (\phi(x_1, t), \dots, \phi(x_N, t))^\top,$$

where $\eta \sim \mathcal{N}(0, 0.01I_N)$. To generate $\phi(x, t)$, we truncate (4.5) at $i = 36$, by keeping only the terms with $\lambda_i \leq 30$ (the sixth repeated eigenvalue of $-\Delta_{S^2}$). Figure 8 contains plots of an example of initial heat configuration with $\zeta = 2$ and the corresponding noisy data for times $t = 0.25$ and $t = 0.4$. Assuming that the center $z^* \in \mathcal{M}_N$, we adopt an optimization perspective to this inverse problem [47] and attempt to maximize the objective function

$$f(z) = -\log \|\mathbf{d} - \mathcal{G}(z)\|_\infty, \quad z \in \mathcal{M}_N,$$



(a) $t = 0$.

(b) $t = 0.25$.

(c) $t = 0.4$.

Figure 8 (a) Initial heat over the point cloud. (b) Noisy evaluation of heat at $t = 0.25$. (c) Noisy evaluation of heat at $t = 0.4$.

along the point cloud \mathcal{M}_N , where $\mathcal{G}(z) \in \mathbb{R}^N$ is the *forward map* given by

$$[\mathcal{G}(z)]_k = \sum_{i=1}^{\infty} \langle \phi_0^z, \psi_i \rangle_{S^2} \cdot e^{-\lambda_i t} \psi_i(x_k), \quad x_k \in \mathcal{M}_N,$$

with $\phi_0^z(x) = \exp(\zeta z^\top x)$ for $x \in S^2$. However, since \mathcal{M} is only known through \mathcal{M}_N , the eigenvalue and eigenfunctions should be also treated as unknown to us. Therefore, we shall instead maximize the approximate objective function

$$f_N(z) = -\log \|\mathbf{d} - \mathcal{G}_N(z)\|_{\infty}, \quad z \in \mathcal{M}_N,$$

where

$$\mathcal{G}_N(z) = \sum_{i=1}^{k_N} \langle \phi_{0,N}^z, \psi_{N,i} \rangle \cdot e^{-\lambda_{N,i} t} \psi_{N,i}, \quad \phi_{0,N}^z = \left(\exp(\zeta z^\top x_1), \dots, \exp(\zeta z^\top x_N) \right)^\top$$

with the hope that the optimizer of f_N agrees with, or at least is close to, that of f . Here, as before, $\{(\lambda_{N,i}, \psi_{N,i})\}_{i=1}^{k_N}$ are eigenpairs of the unnormalized graph Laplacian and $\langle \cdot, \cdot \rangle$ is the standard Euclidean inner product. For the truncation level, we set $k_N = 70$ to account for the discrepancy—shown in Figure 1—between the spectrum of the graph Laplacian and that of the negative Laplace-Beltrami operator.

To optimize f_N , we apply Algorithm 2.1 with a graph Matérn prior (4.2) with parameters $s = 4$, $\kappa = 1$. There is no observation noise in this case since f_N can be computed exactly, so that $\mu_{N,\ell}$ and $\sigma_{N,\ell}$ in the acquisition function will be computed using (2.4) with $\sigma = 0$ and $Y_\ell = (f_N(z_1), \dots, f_N(z_\ell))^\top$. Since we are interested in the recovery of z^* , we shall report the distance measure $\|z^* - z_L^*\|_2$, where z_L^* is the query point returned by GGP-UCB or random sampling that maximizes f_N in the first L iterations. The results are shown in Figure 9 for observations \mathbf{d} collected at two different times $t = 0.25$ and $t = 0.4$. Qualitatively similar performance as in previous examples is achieved. However, notice that in Figure 9b the recovery is not exact, as the distance $\|z^* - z_L^*\|_2$ does not decrease to zero. This is because we are searching for the maximizer of the approximate objective f_N , which differs from the true heat source z^* when t is large due to the approximation error of \mathcal{G}_N to \mathcal{G} . In other words, the attainable discrepancy, defined as the distance

between z^* and the maximizer of f_N , is nonzero in this case. Besides this effect caused by an error in the approximation of the objective, the simulation results suggest that our GGP-UCB algorithm correctly finds the maximizer of the approximate objective f_N with a significantly smaller number L of queries than the total number N of points in \mathcal{M}_N .

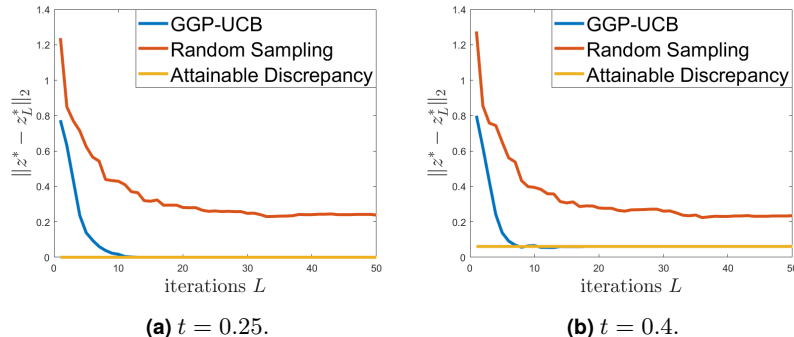


Figure 9 Comparison of $\|z^* - z_L^*\|_2$ (cf. (2.1)) between GGP-UCB and random sampling for (a) $t = 0.25$ and (b) $t = 0.4$. The results are averaged over 50 trials.

We remark that there are two intertwined aspects which make source detection difficult for intermediate to large t values. The smoothing effect of the forward map \mathcal{G} implies that a larger observation time will lead to a more flattened (homogeneous) temperature configuration, as shown in Figure 8. In other words, two rather different initial heat configurations will yield almost identical heat configurations after a large time $t > 0$. Such ill-posedness hinders the recovery of the true heat source location for large t . In addition, the forward map \mathcal{G} and its approximation \mathcal{G}_N are defined in terms of an exponential transformation of the eigenvalues of the Laplace-Beltrami operator and the graph Laplacian. Therefore, for moderate t , any small inaccuracy in the eigenvalue estimation can lead to significantly different forward models \mathcal{G} and \mathcal{G}_N , so that f_N is a poor approximation to f . If one had access to the true forward map, this issue would not be present.

5 Discussion

This paper introduced GGP-UCB, a manifold learning technique to optimize an objective function on a hidden manifold. Our regret bounds and numerical experiments demonstrate the effectiveness of our method. Similar to other Bayesian nonparametric techniques, we expect GGP-UCB to be particularly effective when the dimension m of the manifold $\mathcal{M} \subset \mathbb{R}^d$ is small or moderate. In particular, our regret bounds in Theorem 2.4 suffer from the standard curse of dimension with m , while they do not depend on the dimension d of the ambient space.

For simplicity, we have assumed that the dimension m of \mathcal{M} is known, that we have access to clean samples from \mathcal{M} , and that \mathcal{M} has no boundary. If the dimension of \mathcal{M} is unknown, classical manifold learning techniques can be used to estimate it [33, 31]. Similarly, if the given point cloud is noisy in that it consists of random perturbations of points sampled from \mathcal{M} , a denoising method can be employed to uncover the underlying geometry [24]. Finally, if \mathcal{M} has a boundary, our GGP-UCB method may be combined with a ghost point diffusion map algorithm to remove boundary artifacts [32, 44, 37].

We have focused on GGP surrogate models defined via a specific choice of unnormalized graph-Laplacian; other graph constructions (e.g. based on nearest neighbors or self-tuning kernels)

and graph-Laplacian (e.g. symmetric and random walk) could be considered [53]. Our focus on UCB acquisition functions was motivated by the desire to establish convergence guarantees under misspecification, as well as by their simplicity and successful empirical performance. However, algorithmically there is no roadblock in employing other acquisition functions such as expected improvement and Thompson sampling. An interesting direction for future research is to investigate correction for misspecification for these alternatives and integrate them into our framework for optimizing functions over manifolds.

Acknowledgments

DSA is thankful for the support of NSF DMS-2027056 and DOE DE-SC0022232. DSA is also thankful to the BBVA Foundation for a start-up grant. The authors are grateful to Jiaheng Chen for generous feedback on an earlier version of this manuscript.

References

- [1] P.-A. Absil, R. Mahony, and R. Sepulchre. *Optimization Algorithms on Matrix Manifolds*. Princeton University Press, 2009.
- [2] R. Baptista and M. Poloczek. Bayesian optimization of combinatorial structures. In *International Conference on Machine Learning*, pages 462–471. PMLR, 2018.
- [3] V. I. Bogachev. *Gaussian Measures*. Number 62 in Mathematical Surveys and Monographs. American Mathematical Soc., 1998.
- [4] I. Bogunovic and A. Krause. Misspecified Gaussian process bandit optimization. *Advances in Neural Information Processing Systems*, 34:3004–3015, 2021.
- [5] D. Bolin and K. Kirchner. The rational SPDE approach for Gaussian random fields with general smoothness. *Journal of Computational and Graphical Statistics*, 29(2):274–285, 2020.
- [6] V. Borovitskiy, A. Terenin, P. Mostowsky, et al. Matérn Gaussian processes on Riemannian manifolds. *Advances in Neural Information Processing Systems*, 33:12426–12437, 2020.
- [7] V. Borovitskiy, I. Azangulov, A. Terenin, P. Mostowsky, M. Deisenroth, and N. Durrande. Matérn Gaussian processes on graphs. In *International Conference on Artificial Intelligence and Statistics*, pages 2593–2601. PMLR, 2021.
- [8] N. Boumal. *An Introduction to Optimization on Smooth Manifolds*. To appear in Cambridge University Press, Available online, 2020.
- [9] E. Brochu, V. M. Cora, and N. De Freitas. A tutorial on Bayesian optimization of expensive cost functions, with application to active user modeling and hierarchical reinforcement learning. *arXiv preprint arXiv:1012.2599*, 2010.
- [10] A. D. Bull. Convergence rates of efficient global optimization algorithms. *Journal of Machine Learning Research*, 12(10), 2011.
- [11] Y. Canzani. Analysis on manifolds via the Laplacian. *Lecture Notes available at: <http://www.math.harvard.edu/canzani/docs/Laplacian.pdf>*, 2013.

- [12] H. A. Chipman, E. I. George, and R. E. McCulloch. Bart: Bayesian additive regression trees. *The Annals of Applied Statistics*, 4(1):266–298, 2010.
- [13] K. Crane. Keenan’s 3d model repository. URL <http://www.cs.cmu.edu/~kmcrane/Projects/ModelRepository>.
- [14] N. De Freitas, A. J. Smola, and M. Zoghi. Exponential regret bounds for Gaussian process bandits with deterministic observations. In *International Conference on Machine Learning*, pages 955–962, 2012.
- [15] A. Deshwal, S. Belakaria, and J. R. Doppa. Bayesian optimization over hybrid spaces. In *International Conference on Machine Learning*, pages 2632–2643. PMLR, 2021.
- [16] H. Donnelly. Eigenfunctions of the Laplacian on compact Riemannian manifolds. *Asian Journal of Mathematics*, 10(1):115–126, 2006.
- [17] D. B. Dunson, H.-T. Wu, N. Wu, et al. Graph based Gaussian processes on restricted domains. *Journal of the Royal Statistical Society Series B*, 84(2):414–439, 2022.
- [18] A. Edelman, T. A. Arias, and S. T. Smith. The geometry of algorithms with orthogonality constraints. *SIAM Journal on Matrix Analysis and Applications*, 20(2):303–353, 1998.
- [19] A. Feragen, F. Lauze, and S. Hauberg. Geodesic exponential kernels: When curvature and linearity conflict. In *Proceedings of the IEEE conference on computer vision and pattern recognition*, pages 3032–3042, 2015.
- [20] R. A. Fisher. Dispersion on a sphere. *Proceedings of the Royal Society of London. Series A. Mathematical and Physical Sciences*, 217(1130):295–305, 1953.
- [21] P. I. Frazier. A tutorial on Bayesian optimization. *arXiv preprint arXiv:1807.02811*, 2018.
- [22] T. Gao, S. Z. Kovalsky, and I. Daubechies. Gaussian process landmarking on manifolds. *SIAM Journal on Mathematics of Data Science*, 1(1):208–236, 2019.
- [23] N. Garcia Trillos and D. Sanz-Alonso. Continuum limits of posteriors in graph Bayesian inverse problems. *SIAM Journal on Mathematical Analysis*, 50(4):4020–4040, 2018.
- [24] N. Garcia Trillos, D. Sanz-Alonso, and R. Yang. Local regularization of noisy point clouds: Improved global geometric estimates and data analysis. *Journal of Machine Learning Research*, 20(136):1–37, 2019.
- [25] N. Garcia Trillos, M. Gerlach, M. Hein, and D. Slepčev. Error estimates for spectral convergence of the graph Laplacian on random geometric graphs toward the Laplace–Beltrami operator. *Foundations of Computational Mathematics*, 20(4):827–887, 2020.
- [26] N. Garcia Trillos, Z. Kaplan, T. Samakhoana, and D. Sanz-Alonso. On the consistency of graph-based Bayesian semi-supervised learning and the scalability of sampling algorithms. *Journal of Machine Learning Research*, 21(28):1–47, 2020.

- [27] N. Garcia Trillos, D. Sanz-Alonso, and R. Yang. Mathematical foundations of graph-based Bayesian semi-supervised learning. *arXiv preprint arXiv:2207.01093*, 2022.
- [28] T. Gneiting. Strictly and non-strictly positive definite functions on spheres. *Bernoulli*, 19(4):1327–1349, 2013.
- [29] R. B. Gramacy. *Surrogates: Gaussian Process Modeling, Design, and Optimization for the Applied Sciences*. Chapman and Hall/CRC, 2020.
- [30] S. Grünewälder, J.-Y. Audibert, M. Opper, and J. Shawe-Taylor. Regret bounds for Gaussian process bandit problems. In *Proceedings of the Thirteenth International Conference on Artificial Intelligence and Statistics*, pages 273–280, 2010.
- [31] J. Harlim, D. Sanz-Alonso, and R. Yang. Kernel methods for Bayesian elliptic inverse problems on manifolds. *SIAM/ASA Journal on Uncertainty Quantification*, 8(4):1414–1445, 2020.
- [32] J. Harlim, S. W. Jiang, H. Kim, and D. Sanz-Alonso. Graph-based prior and forward models for inverse problems on manifolds with boundaries. *Inverse Problems*, 38(3):035006, 2022.
- [33] M. Hein and J.-Y. Audibert. Intrinsic dimensionality estimation of submanifolds in \mathbb{R}^d . In *Proceedings of the 22nd International Conference on Machine Learning*, pages 289–296, 2005.
- [34] J. Hu, X. Liu, Z.-W. Wen, and Y.-X. Yuan. A brief introduction to manifold optimization. *Journal of the Operations Research Society of China*, 8(2):199–248, 2020.
- [35] N. Jaquier, L. Rozo, S. Calinon, and M. Bürger. Bayesian optimization meets Riemannian manifolds in robot learning. In *Conference on Robot Learning*, pages 233–246. PMLR, 2020.
- [36] N. Jaquier, V. Borovitskiy, A. Smolenskiy, A. Terenin, T. Asfour, and L. Rozo. Geometry-aware Bayesian optimization in robotics using Riemannian Matérn kernels. In *Conference on Robot Learning*, pages 794–805. PMLR, 2022.
- [37] S. W. Jiang and J. Harlim. Ghost point diffusion maps for solving elliptic PDEs on manifolds with classical boundary conditions. *Communications on Pure and Applied Mathematics*, 2020.
- [38] K. Kawaguchi, L. P. Kaelbling, and T. Lozano-Pérez. Bayesian optimization with exponential convergence. *Advances in Neural Information Processing Systems*, 28, 2015.
- [39] A. Lang, J. Potthoff, M. Schlather, and D. Schwab. Continuity of random fields on Riemannian manifolds. *Communications on Stochastic Analysis*, 10(2):4, 2016.
- [40] D. Li, W. Tang, and S. Banerjee. Inference for Gaussian processes with Matérn covariogram on compact Riemannian manifolds. *arXiv preprint arXiv:2104.03529*, 2021.
- [41] F. Lindgren, H. Rue, and J. Lindström. An explicit link between Gaussian fields and Gaussian Markov random fields: the stochastic partial differential equation approach. *Journal of the Royal Statistical Society: Series B (Statistical Methodology)*, 73(4):423–498, 2011.

- [42] P. Luong, S. Gupta, D. Nguyen, S. Rana, and S. Venkatesh. Bayesian optimization with discrete variables. In *Australasian Joint Conference on Artificial Intelligence*, pages 473–484. Springer, 2019.
- [43] J. Mockus, V. Tiesis, and A. Zilinskas. The application of Bayesian methods for seeking the extremum. *Towards global optimization*, 2(117-129):2, 1978.
- [44] J. W. Peoples and J. Harlim. Spectral convergence of symmetrized graph Laplacian on manifolds with boundary. *arXiv preprint arXiv:2110.06988*, 2021.
- [45] D. Sanz-Alonso and R. Yang. The SPDE approach to Matérn fields: Graph representations. *To appear in Statistical Science*, 2022.
- [46] D. Sanz-Alonso and R. Yang. Unlabeled data help in graph-based semi-supervised learning: a Bayesian nonparametrics perspective. *Journal of Machine Learning Research*, 23(97):1–28, 2022.
- [47] D. Sanz-Alonso, A. M. Stuart, and A. Taeb. *Inverse Problems and Data Assimilation*. arXiv:1810.06191, 2022.
- [48] B. Shahriari, K. Swersky, Z. Wang, R. P. Adams, and N. De Freitas. Taking the human out of the loop: A review of Bayesian optimization. *Proceedings of the IEEE*, 104(1):148–175, 2015.
- [49] N. Srinivas, A. Krause, S. Kakade, and M. Seeger. Gaussian process optimization in the bandit setting: No regret and experimental design. In *Proceedings of the 27th International Conference on Machine Learning*, 2010.
- [50] K. Swersky, Y. Rubanova, D. Dohan, and K. Murphy. Amortized Bayesian optimization over discrete spaces. In *Conference on Uncertainty in Artificial Intelligence*, pages 769–778. PMLR, 2020.
- [51] S. Vakili, K. Khezeli, and V. Picheny. On information gain and regret bounds in Gaussian process bandits. In *International Conference on Artificial Intelligence and Statistics*, pages 82–90. PMLR, 2021.
- [52] E. Vazquez and J. Bect. Convergence properties of the expected improvement algorithm with fixed mean and covariance functions. *Journal of Statistical Planning and Inference*, 140(11):3088–3095, 2010.
- [53] U. Von Luxburg. A tutorial on spectral clustering. *Statistics and Computing*, 17(4):395–416, 2007.
- [54] P. Whittle. Stochastic-processes in several dimensions. *Bulletin of the International Statistical Institute*, 40(2):974–994, 1963.
- [55] C. K. I. Williams and C. E. Rasmussen. *Gaussian Processes for Machine Learning*, volume 2 of 3. MIT Press Cambridge, MA, 2006.

- [56] B. Xu. Asymptotic behavior of L^2 -normalized eigenfunctions of the Laplace-Beltrami operator on a closed Riemannian manifold. *Harmonic Analysis and its Applications*, pages 99–117, 2006.
- [57] K. Ye, K. S.-W. Wong, and L.-H. Lim. Optimization on flag manifolds. *Mathematical Programming*, 194(1):621–660, 2022.
- [58] H. Zhang. Inconsistent estimation and asymptotically equal interpolations in model-based geostatistics. *Journal of the American Statistical Association*, 99(465):250–261, 2004.
- [59] H. Zhang and S. X. Chen. Concentration inequalities for statistical inference. *arXiv preprint arXiv:2011.02258*, 2020.

This appendix contains the proofs of Proposition 2.3 and Theorem 2.4. The proofs build on the theory of spectral convergence of graph Laplacians and regret analysis of Bayesian optimization algorithms. To make our presentation self-contained, we will introduce necessary background and previous results whenever needed.

A Proof of Proposition 2.3

Let \mathcal{M}_N be i.i.d. samples from a distribution μ supported on a smooth, connected, and compact m -dimensional submanifold $\mathcal{M} \subset \mathbb{R}^d$ without boundary. For simplicity, we shall assume that μ is the uniform distribution on \mathcal{M} . The first result [25, Theorem 2] states that with high probability, the x_i 's form a ρ_N -net over \mathcal{M} and characterizes ρ_N .

Proposition A.1. *For any $c > 1$, with probability $1 - O(N^{-c})$, there exists a transportation map $T_N : \mathcal{M} \rightarrow \{x_1, \dots, x_N\}$ so that*

$$\rho_N := \sup_{x \in \mathcal{M}} d_{\mathcal{M}}(x, T_N(x)) \lesssim \frac{(\log N)^{p_m}}{N^{1/m}}, \quad (\text{A.1})$$

where $p_m = 3/4$ when $m = 2$ and $p_m = 1/m$ otherwise. We recall that $d_{\mathcal{M}}$ is the geodesic distance on \mathcal{M} .

Proposition A.1 implies that the point cloud \mathcal{M}_N is “well-structured” with high probability and is the building block for the spectral approximation results below [46, Proposition 10 and Lemma 15]. Recall that the graph-Laplacian Δ_N constructed in Subsection 2.3 admits a spectral decomposition, in analogy to the Laplace-Beltrami operator $\Delta_{\mathcal{M}}$.

Proposition A.2. *Suppose there exists $\delta > 0$ such that, for N sufficiently large,*

$$h_N \gtrsim N^{-\frac{1}{m+4+\delta}}, \quad k_N \lesssim N^{\frac{1-\delta}{m}}, \quad h_N k_N^{\frac{2}{m}} \lesssim 1. \quad (\text{A.2})$$

Then with probability $1 - O(N^{-c})$ for some $c > 0$, there exists orthonormalized eigenfunctions $\{\psi_{N,i}\}_{i=1}^N$ for Δ_N , $\{\psi_i\}_{i=1}^{\infty}$ for $\Delta_{\mathcal{M}}$, and $T_N : \mathcal{M} \rightarrow \{x_1, \dots, x_N\}$ satisfying $T_N(x_i) = x_i$ so that, for $i = 1, \dots, k_N$,

$$\begin{aligned} |\lambda_{N,i} - \lambda_i| &\lesssim \lambda_i \left(\frac{\rho_N}{h_N} + h_N \sqrt{\lambda_i} \right), \\ \|\psi_{N,i} \circ T_N - \psi_i\|_{\infty} &\lesssim \lambda_i^{m+1} i^{\frac{3}{2}} \sqrt{\frac{\rho_N}{h_N} + h_N \sqrt{\lambda_i}}. \end{aligned}$$

We also need a result on the growth of the L^∞ -norm of the Laplace-Beltrami eigenfunctions and their gradients from [16, Theorem 1.2] and [56, equation (2.10)].

Proposition A.3. *Let ψ be an L^2 -normalized eigenfunction of $-\Delta_{\mathcal{M}}$ associated with $\lambda \neq 0$. Then $\|\psi\|_\infty \leq C\lambda^{(m-1)/4}$ and $\|\nabla\psi\|_\infty \leq C\lambda^{(m+1)/2}$ for a universal constant C .*

Lemma A.4. *The random field u^{SE} defined in (2.7) satisfies $\mathbb{E}\|u^{\text{SE}}\|_{L^2}^2 \asymp 1$ and is almost surely continuous.*

Proof. By Weyl's law that $\lambda_i \asymp i^{\frac{2}{m}}$ (see e.g. [11, Theorem 72]), we have

$$\mathbb{E} \left\| \sum_{i=1}^{\infty} e^{-\frac{\lambda_i \tau}{2}} \xi_i \psi_i \right\|_{L^2}^2 = \sum_{i=1}^{\infty} e^{-\lambda_i \tau} \asymp \sum_{i=1}^{\infty} e^{-Ci^{2/m}\tau} \asymp \int_0^\infty e^{-Cx^{2/m}\tau} dx.$$

By a change of variable, the last expression is equal to

$$\frac{m}{2} \int_0^\infty e^{-C\tau x} x^{\frac{m}{2}-1} dx = \frac{m}{2} \cdot \frac{\Gamma(\frac{m}{2})}{(C\tau)^{m/2}} \asymp \tau^{-\frac{m}{2}}.$$

For the second claim, by [39, Corollary 4.5] it suffices to show that

$$\mathbb{E}|u^{\text{SE}}(x) - u^{\text{SE}}(y)|^2 \leq Cd_{\mathcal{M}}(x, y)^\eta \tag{A.3}$$

for some $\eta \in (0, 1)$, $C > 0$, and for all x, y satisfying $d_{\mathcal{M}}(x, y) < 1$. Notice that

$$\begin{aligned} \mathbb{E}|u^{\text{SE}}(x) - u^{\text{SE}}(y)|^2 &= \tau^{\frac{m}{2}} \mathbb{E} \left| \sum_{i=1}^{\infty} e^{-\frac{\lambda_i \tau}{2}} \xi_i (\psi_i(x) - \psi_i(y)) \right|^2 \\ &= \tau^{\frac{m}{2}} \sum_{i=1}^{\infty} e^{-\lambda_i \tau} |\psi_i(x) - \psi_i(y)|^2 \\ &\leq \tau^{\frac{m}{2}} \sum_{i=1}^{\infty} e^{-\lambda_i \tau} \|\nabla\psi_i\|_\infty^2 d_{\mathcal{M}}(x, y)^2 \leq C\tau^{\frac{m}{2}} \sum_{i=1}^{\infty} e^{-\lambda_i \tau} \lambda_i^{m+1} d_{\mathcal{M}}(x, y)^2, \end{aligned}$$

where we have used Proposition A.3 in the last step. Now by Weyl's law,

$$\sum_{i=1}^{\infty} e^{-\lambda_i \tau} \lambda_i^{m+1} \leq C \sum_{i=1}^{\infty} e^{-c\tau i^{2/m}} i^{\frac{2(m+1)}{m}} \leq C \int_1^\infty e^{-c\tau x^{2/m}} x^{\frac{2(m+1)}{m}} dx < \infty.$$

Therefore,

$$\mathbb{E}|u^{\text{SE}}(x) - u^{\text{SE}}(y)|^2 \leq Cd_{\mathcal{M}}(x, y)^2 \leq Cd_{\mathcal{M}}(x, y)^\eta$$

for any $\eta \in (0, 1)$ when $d_{\mathcal{M}}(x, y) < 1$, thereby verifying (A.3). \square

Now we are ready to prove Proposition 2.3. The first statement on the approximation error of u_N^{Ma} follows from [46, Theorem 4.6]. To show the second, recall that

$$\begin{aligned} u_N^{\text{SE}} &= \tau^{\frac{m}{4}} \sum_{i=1}^{k_N} e^{-\frac{\lambda_{N,i}\tau}{2}} \xi_i \psi_{N,i}, & \xi_i &\stackrel{i.i.d.}{\sim} \mathcal{N}(0, 1), \\ u^{\text{SE}} &= \tau^{\frac{m}{4}} \sum_{i=1}^{\infty} e^{-\frac{\lambda_i \tau}{2}} \xi_i \psi_i, & \xi_i &\stackrel{i.i.d.}{\sim} \mathcal{N}(0, 1), \end{aligned}$$

and introduce two intermediate random processes

$$\begin{aligned}\tilde{u}_N^{\text{SE}} &= \tau^{\frac{m}{4}} \sum_{i=1}^{k_N} e^{-\frac{\lambda_i \tau}{2}} \xi_i \psi_{N,i}, & \xi_i &\stackrel{i.i.d.}{\sim} \mathcal{N}(0, 1), \\ \hat{u}_N^{\text{SE}} &= \tau^{\frac{m}{4}} \sum_{i=1}^{k_N} e^{-\frac{\lambda_i \tau}{2}} \xi_i \psi_i, & \xi_i &\stackrel{i.i.d.}{\sim} \mathcal{N}(0, 1).\end{aligned}$$

We then have

$$\mathbb{E} \|u_N^{\text{SE}} \circ T_N - u^{\text{SE}}\|_\infty \leq \mathbb{E} \|u_N^{\text{SE}} \circ T_N - \tilde{u}_N^{\text{SE}} \circ T_N\|_\infty + \mathbb{E} \|\tilde{u}_N^{\text{SE}} \circ T_N - \hat{u}_N^{\text{SE}}\|_\infty + \mathbb{E} \|\hat{u}_N^{\text{SE}} - u^{\text{SE}}\|_\infty$$

and we shall proceed by bounding each of the three terms on the right. First, note that

$$\mathbb{E} \|\hat{u}_N^{\text{SE}} - u^{\text{SE}}\|_\infty = \mathbb{E} \left\| \tau^{\frac{m}{4}} \sum_{i=k_N+1}^{\infty} e^{-\frac{\lambda_i \tau}{2}} \xi_i \psi_i \right\|_\infty \lesssim \sum_{i=k_N+1}^{\infty} e^{-\frac{\lambda_i \tau}{2}} \mathbb{E} |\xi_i| \|\psi_i\|_\infty \lesssim \sum_{i=k_N+1}^{\infty} e^{-\frac{\lambda_i \tau}{2}} \lambda_i^{\frac{m-1}{4}}, \quad (\text{A.4})$$

where we have used Proposition A.3 in the last step. Now by Weyl's law, $\lambda_i \asymp i^{2/m}$ so that we can further bound

$$(\text{A.4}) \lesssim \sum_{i=k_N+1}^{\infty} e^{-c_0 \tau i^{2/m}} i^{\frac{2}{m} \frac{m-1}{4}} \lesssim \int_{k_N}^{\infty} e^{-c_0 \tau x^{2/m}} x^{\frac{m-1}{2m}} dx = \int_{k_N^{2/m}}^{\infty} e^{-c_0 \tau z} z^{\frac{3m-1}{4}-1} dz \quad (\text{A.5})$$

after a change of variable, where c_0 is a universal constant. Notice that the rightmost term (A.5) is equal up to a multiplicative constant to $\mathbb{P}(X \geq k_N^{2/m})$ with X being a Gamma random variable with shape parameter $\frac{3m-1}{4}$ and scale parameter $\frac{1}{c_0 \tau}$. Now by the tail bound of sum-Gamma distributions (cf. [59, Lemma 5.1]) applied to $X - \mathbb{E}X \in \text{sub}\Gamma\left(\frac{3m-1}{4c_0^2 \tau^2}, \frac{1}{c_0 \tau}\right)$, we have

$$\mathbb{E} \|\hat{u}_N^{\text{SE}} - u^{\text{SE}}\|_\infty \lesssim (\text{A.5}) \lesssim \mathbb{P}(X - \mathbb{E}X \geq k_N^{2/m} - \mathbb{E}X) \lesssim e^{-C k_N^{2/m}} \quad (\text{A.6})$$

for some constant C when $k_N^{2/m} \gg \mathbb{E}X = \frac{3m-1}{c_0 \tau}$. Similarly, we have

$$\mathbb{E} \|u_N^{\text{SE}} \circ T_N - \tilde{u}_N^{\text{SE}} \circ T_N\|_\infty \lesssim \sum_{i=1}^{k_N} \left| e^{-\frac{\lambda_{N,i} \tau}{2}} - e^{-\frac{\lambda_i \tau}{2}} \right| \|\psi_{N,i} \circ T_N\|_\infty. \quad (\text{A.7})$$

By the mean value theorem, we have that $|e^{-x} - e^{-y}| = e^{-\zeta} |x - y| \leq \max\{e^{-x}, e^{-y}\} |x - y|$ for some $\zeta \in (\min(x, y), \max(x, y))$ where $x, y > 0$. Thus, we have

$$\left| e^{-\frac{\lambda_{N,i} \tau}{2}} - e^{-\frac{\lambda_i \tau}{2}} \right| \leq \max\left\{ e^{-\frac{\lambda_{N,i} \tau}{2}}, e^{-\frac{\lambda_i \tau}{2}} \right\} \frac{\tau}{2} |\lambda_{N,i} - \lambda_i| \leq \frac{\tau}{2} e^{-\frac{\lambda_i \tau}{4}} \lambda_i \left(\frac{\rho_N}{h_N} + h_N \sqrt{\lambda_i} \right),$$

where in the last step we have used Proposition A.2 which also implies $\lambda_{N,i} \geq \lambda_i/2$ when N is large. Moreover, Proposition A.2 implies that, for $i = 1, \dots, k_N$,

$$\begin{aligned}\|\psi_{N,i} \circ T_N\|_\infty &\leq \|\psi_{N,i} \circ T_N - \psi_i\|_\infty + \|\psi_i\|_\infty \\ &\lesssim \lambda_i^{m+1} i^{\frac{3}{2}} \sqrt{\frac{\rho_N}{h_N} + h_N \sqrt{\lambda_i}} + \|\psi_i\|_\infty \lesssim \left(\frac{\rho_N}{h_N} + h_N \right) i^{\frac{7m+5}{2m}} + \|\psi_i\|_\infty.\end{aligned} \quad (\text{A.8})$$

Proposition A.3 implies that $\|\psi_i\|_\infty \lesssim \lambda_i^{\frac{m-1}{4}} \lesssim i^{\frac{m-1}{2m}}$. Therefore we would like to set h_N and k_N to satisfy

$$\left(\frac{\rho_N}{h_N} + h_N\right) k_N^{\frac{7m+5}{2m}} \lesssim k_N^{\frac{m-1}{2m}} \quad (\text{A.9})$$

so that (A.8) grows like $\|\psi_i\|_\infty$ for all $i = 1, \dots, k_N$. We shall keep (A.9) in mind together with those conditions in (A.2) and proceed by assuming that we have made such choices. Now we can bound

$$(\text{A.7}) \lesssim \sum_{i=1}^{k_N} \frac{\tau}{2} e^{-\frac{\lambda_i \tau}{4}} \lambda_i^{\frac{m+3}{4}} \left(\frac{\rho_N}{h_N} + h_N \sqrt{\lambda_i}\right) \lesssim \frac{\tau}{2} \left(\frac{\rho_N}{h_N} + h_N\right) \sum_{i=1}^{k_N} e^{-\frac{\lambda_i \tau}{4}} \lambda_i^{\frac{m+5}{4}} \lesssim \frac{\rho_N}{h_N} + h_N, \quad (\text{A.10})$$

where we used the fact that

$$\sum_{i=1}^{k_N} e^{-\frac{\lambda_i \tau}{4}} \lambda_i^{\frac{m+5}{4}} \lesssim \sum_{i=1}^{k_N} e^{-C i^{2/m}} i^{\frac{m+5}{2m}} \lesssim \int_1^\infty e^{-C x^{2/m}} x^{\frac{m+5}{2m}} dx < \infty.$$

Lastly, we have by Proposition A.2

$$\mathbb{E} \|\tilde{u}_N^{\text{SE}} \circ T_N - \hat{u}_N^{\text{SE}}\|_\infty \lesssim \sum_{i=1}^{k_N} e^{-\frac{\lambda_i \tau}{2}} \|\psi_{N,i} \circ T_N - \psi_i\|_\infty \quad (\text{A.11})$$

$$\lesssim \sum_{i=1}^{k_N} e^{-\frac{\lambda_i \tau}{2}} \lambda_i^{m+1} i^{\frac{3}{2}} \sqrt{\frac{\rho_N}{h_N} + h_N \sqrt{\lambda_i}} \lesssim \sqrt{\frac{\rho_N}{h_N} + h_N}. \quad (\text{A.12})$$

Combining (A.6), (A.10), (A.12), we get

$$\mathbb{E} \|u_N^{\text{SE}} \circ T_N - u^{\text{SE}}\|_\infty \lesssim e^{-C k_N^{2/m}} + \sqrt{\frac{\rho_N}{h_N} + h_N}.$$

Now it remains to set h_N and k_N and we remark that the approximation error will be dominated by the second term $\sqrt{\rho_N/h_N + h_N}$ when N is large. It can be checked that the following scaling satisfies the conditions imposed by (A.2) and (A.9).

Case 1: $m \leq 4$ Setting for some arbitrarily small $\delta > 0$

$$h_N \asymp N^{-\frac{1}{m+4+\delta}} (\log N)^{\frac{pm}{2}}, \quad (\log N)^{\frac{m}{2}} \ll k_N \ll N^{\frac{m}{(m+4+\delta)(3m+3)}} (\log N)^{-\frac{mpm}{6m+6}},$$

we obtain that, for large N ,

$$\mathbb{E} \|u_N^{\text{SE}} \circ T_N - u^{\text{SE}}\|_\infty \lesssim N^{-\frac{1}{2(m+4+\delta)}} (\log N)^{\frac{pm}{4}}.$$

Case 2: $m \geq 5$ Setting

$$h_N \asymp N^{-\frac{1}{2m}} (\log N)^{-\frac{pm}{2}}, \quad (\log N)^{\frac{m}{2}} \ll k_N \ll N^{\frac{1}{6m+6}} (\log N)^{-\frac{mpm}{6m+6}},$$

we obtain

$$\mathbb{E} \|u_N^{\text{SE}} \circ T_N - u^{\text{SE}}\|_\infty \lesssim N^{-\frac{1}{4m}} (\log N)^{\frac{pm}{4}}.$$

B Proof of Theorem 2.4

We start by introducing the key ingredients of the regret analysis of Bayesian optimization algorithms, in particular the GGP-UCB algorithm. Most of the preliminary results in this section can be found in [49, 4].

Recall that our goal is to bound the simple regret defined as in (2.1). But a typical strategy in the BO literature is to look at the *cumulative regret*, defined as

$$R_{N,L} = \sum_{\ell=1}^L \left(f(z^*) - f(z_\ell) \right), \quad z^* = \arg \max_{z \in \mathcal{M}_N} f(z). \quad (\text{B.1})$$

Then using the fact that

$$f(z_L^*) \geq \frac{1}{L} \sum_{\ell=1}^L f(z_\ell), \quad z_L^* = \arg \max_{z \in \{z_\ell\}_{\ell=1}^L} f(z),$$

one can bound the simple regret as

$$r_{N,L} = f(z^*) - f(z_L^*) \leq \frac{1}{L} \sum_{\ell=1}^L \left(f(z^*) - f(z_\ell) \right) = \frac{R_{N,L}}{L}. \quad (\text{B.2})$$

The key to bounding the cumulative regret consists of two steps. The first is a concentration-type result that constructs confidence bands which f lies in with high probability based on the observed samples. More precisely, we have the following result.

Lemma B.1. *Let $\delta \in (0, 1)$ and set $b_{N,\ell} = \sqrt{2 \log(\pi^2 \ell^2 N / 6\delta)}$. Then with probability $1 - \delta$, we have*

$$|u_N(z) - \tilde{\mu}_{N,\ell-1}(z)| \leq b_{N,\ell} \sigma_{N,\ell-1}(z) \quad \forall z \in \mathcal{M}_N, \quad \forall \ell \geq 1,$$

where

$$\tilde{\mu}_{N,\ell}(z) = c_{N,\ell}(z)^\top (C_{N,\ell} + \sigma^2 I)^{-1} \tilde{Y}_{N,\ell}$$

and $\tilde{Y}_{N,\ell} \in \mathbb{R}^\ell$ is vector with entry $(\tilde{Y}_{N,\ell})_i = u_N(z_i) + \eta_i$. See (2.4) for the definition of $c_{N,\ell}$ and $C_{N,\ell}$.

Proof. This is [49, Lemma 5.1] applied to the graph GP u_N , with the ‘‘surrogate’’ data $\tilde{Y}_{N,\ell}$. \square

Here and below, we shall use $c_N(\cdot, \cdot)$ as a placeholder for either the Matérn or SE graph-based covariance function (2.14). Notice that the ‘‘surrogate’’ data $\tilde{Y}_{N,\ell}$ is introduced only for the purpose of analysis and the algorithm only has access to the real data $y_\ell = f(z_\ell) + \eta_\ell$. An important follow-up question is on the difference between the surrogate-data posterior mean $\tilde{\mu}_{N,\ell}$ and the true posterior mean $\mu_{N,\ell} = c_{N,\ell}(x)^\top (C_{N,\ell} + \sigma^2 I)^{-1} Y_\ell$ that is actually used in the algorithm, answered by the following result.

Lemma B.2. *In the event of (2.16), we have*

$$|\mu_{N,\ell}(z) - \tilde{\mu}_{N,\ell}(z)| \leq \frac{\epsilon_N \sqrt{\ell}}{\delta \sigma} \sigma_{N,\ell}(z), \quad \forall z \in \mathcal{M}_N \quad \forall \ell \geq 1,$$

where we recall σ is the standard deviation of the noise η_ℓ and $\sigma_{N,\ell}$ is defined in (2.4).

Proof. This follows by setting the misspecification error to be ϵ_N/δ in [4, Lemma 2]. \square

Now with these preparations, we are ready to start the proof of Theorem 2.4. In the event of (2.16) that

$$\max_{z \in \mathcal{M}_N} |u_N(z) - f(z)| \leq \delta^{-1} \epsilon_N,$$

which holds with probability $1 - \delta$ by Proposition 2.3 (with ϵ_N the corresponding error bounds (2.15)), we can shift our focus to the following cumulative regret

$$\tilde{R}_{N,L} = \sum_{\ell=1}^L u_N(z^*) - u_N(z_\ell), \quad z^* = \max_{z \in \mathcal{M}_N} u_N(z),$$

which differs from $R_{N,L}$ (B.1) at most by $2\epsilon_N L/\delta$. Under the further event where Lemma B.1 holds, we have by Lemma B.2 that for all $z \in \mathcal{M}_N$,

$$\begin{aligned} \mu_{N,\ell-1}(z) - \left(b_{N,\ell} + \frac{\epsilon_N \sqrt{\ell-1}}{\delta \sigma} \right) \sigma_{N,\ell-1}(z) &\leq u_N(z) \\ &\leq \mu_{N,\ell-1}(z) + \left(b_{N,\ell} + \frac{\epsilon_N \sqrt{\ell-1}}{\delta \sigma} \right) \sigma_{N,\ell-1}(z). \end{aligned}$$

Therefore

$$\begin{aligned} \tilde{R}_{N,L} &\leq \sum_{\ell=1}^L \left(\mu_{N,\ell-1}(z^*) + \left(b_{N,\ell} + \frac{\epsilon_N \sqrt{\ell-1}}{\delta \sigma} \right) \sigma_{N,\ell-1}(z^*) \right. \\ &\quad \left. - \left[\mu_{N,\ell-1}(z_\ell) - \left(b_{N,\ell} + \frac{\epsilon_N \sqrt{\ell-1}}{\delta \sigma} \right) \sigma_{N,\ell-1}(z_\ell) \right] \right) \\ &\leq 2 \sum_{\ell=1}^L \left(b_{N,\ell} + \frac{\epsilon_N \sqrt{\ell-1}}{\delta \sigma} \right) \sigma_{N,\ell-1}(z_\ell) \\ &\leq 2 \left(b_{N,L} + \frac{\epsilon_N \sqrt{L-1}}{\delta \sigma} \right) \sum_{\ell=1}^L \sigma_{N,\ell-1}(z_\ell), \end{aligned}$$

where in the second step we have used our definition of z_ℓ in (2.18) that for all $z \in \mathcal{M}_N$ including z^*

$$\mu_{N,\ell-1}(z_\ell) + \left(b_{N,\ell} + \frac{\epsilon_N \sqrt{\ell-1}}{\delta \sigma} \right) \sigma_{N,\ell-1}(z_\ell) \geq \mu_{N,\ell-1}(z) + \left(b_{N,\ell} + \frac{\epsilon_N \sqrt{\ell-1}}{\delta \sigma} \right) \sigma_{N,\ell-1}(z).$$

Therefore we have arrived at the conclusion that

$$R_{N,L} \leq \frac{2\epsilon_N L}{\delta} + 2 \left(b_{N,L} + \frac{\epsilon_N \sqrt{L-1}}{\delta \sigma} \right) \sum_{\ell=1}^L \sigma_{N,\ell-1}(z_\ell). \quad (\text{B.3})$$

Here comes the second key ingredient in the regret analysis, which is to relate the sum of posterior standard deviations $\sum_{\ell=1}^L \sigma_{N,\ell-1}(z_\ell)$ to the so-called *maximum information gain*. The following result is taken from [49, Lemma 5.3].

Lemma B.3. Let $I(y; v)$ denote the mutual information between two random vectors y and v of the same size. We have

$$I(\tilde{Y}_{N,L}; \{u_N(z_\ell)\}_{\ell=1}^L) = \frac{1}{2} \sum_{\ell=1}^L \log(1 + \sigma^{-2} \sigma_{N,\ell-1}^2(z_\ell)),$$

where $\tilde{Y}_{N,L}$ is the surrogate data defined in Lemma B.1.

As a corollary, we have the following result.

Lemma B.4. For N large, there exists a universal constant B such that $c_N(x, \tilde{x}) \leq B$. Moreover,

$$\sum_{\ell=1}^L \sigma_{N,\ell-1}(z_\ell) \leq \sqrt{2(\sigma^2 + B^2)L\gamma_L},$$

where

$$\gamma_L = \max_{S \subset \mathcal{M}_N, |S|=L} I(\tilde{Y}_{N,S}; u_N(S))$$

is the maximum information gain. Here $u_N(S)$ denotes the vector $\{u_N(s)\}_{s \in S}$ and $\tilde{Y}_{N,S}$ is the associated vector of observations as in Lemma B.1.

Proof. The first statement can be proved in a similar fashion as Proposition 2.3 by bounding the difference $|c_N(z_1, z_2) - c(z_1, z_2)|$ between the graph and manifold covariance functions, and using the fact that the manifold covariance function $c(\cdot, \cdot)$ is uniformly upper bounded (which follows by the control of growth of the Laplace-Beltrami eigenfunctions in Proposition A.3).

For the second statement, notice that $\sigma_{N,\ell-1}(z_\ell) \leq c_N(z_\ell, z_\ell) \leq B$. Using the fact that $(1 + \sigma^{-2} B^2) \log(1 + x) \geq x$ over $[0, \sigma^{-2} B^2]$, we have

$$\begin{aligned} \sum_{\ell=1}^L \sigma_{N,\ell-1}^2(z_\ell) &\leq (\sigma^2 + B^2) \sum_{\ell=1}^L \log(1 + \sigma^{-2} \sigma_{N,\ell-1}^2(z_\ell)) \\ &= 2(\sigma^2 + B^2) I(\{y_\ell\}_{\ell=1}^L; \{f_N(z_\ell)\}_{\ell=1}^L) \leq 2(\sigma^2 + B^2) \gamma_L, \end{aligned}$$

where the equality in the second step follows from Lemma B.3. Finally, by Cauchy-Schwarz inequality we have that $\sum_{\ell=1}^L \sigma_{N,\ell-1}(z_\ell) \leq \sqrt{L \sum_{\ell=1}^L \sigma_{N,\ell-1}^2(z_\ell)}$ and the result follows. \square

Applying Lemma B.4 to (B.3), we get

$$R_{N,L} \leq C \left(b_{N,L} \sqrt{L} + \frac{\epsilon_N L}{\delta \sigma} \right) \sqrt{\gamma_T}, \quad (\text{B.4})$$

where C is a universal constant. Upper bounds on γ_L have been studied extensively in the literature and by [51, Theorem 3 or equation (7)] with $D = k_N$ and $\delta_D = 0$ in our case (which holds because our graph kernel only has k_N nonzero eigenvalues), we get

$$R_{N,L} \leq C \left(b_{N,L} \sqrt{L} + \frac{\epsilon_N L}{\delta \sigma} \right) \sqrt{k_N \log L}.$$

Finally, we return to bounding the simple regret using (B.2):

$$r_{N,L} \leq \frac{R_{N,L}}{L} \leq C \left(\frac{b_{N,L}}{\sqrt{L}} + \frac{\epsilon_N}{\delta \sigma} \right) \sqrt{k_N \log L}.$$